# Burst Testing of Filament-Wound Graphite-Epoxy Composite Cylindrical Tubes

1 November 2002

Prepared by

D. J. CHANG, H. A. KATZMAN, J. P. NOKES, P. M. ADAMS, S. T. AMIMOTO, P. R. VALENZUELA, T. V. ALBRIGHT, and P. L. JOSEPH Space Materials Laboratory Laboratory Operations

P. B. POLLOCK, B. A. COULTER, and J. K. RATNER Structures Department Structural Mechanics Subdivision

Prepared for

SPACE AND MISSILE SYSTEMS CENTER AIR FORCE SPACE COMMAND 2430 E. El Segundo Boulevard Los Angeles Air Force Base, CA 90245

Space Systems Group

APPROVED FOR PUBLIC RELEASE; DISTRIBUTION UNLIMITED



This report was submitted by The Aerospace Corporation, El Segundo, CA 90245-4691, under Contract No. F04701-00-C-0009 with the Space and Missile Systems Center, 2430 E. El Segundo Blvd., Los Angeles Air Force Base, CA 90245. It was reviewed and approved for The Aerospace Corporation by P. D. Fleischauer, Principal Director, Space Materials Laboratory; E. R. Scheyhing, Principal Director, Structural Mechanics Subdivision; and W. H. Huber, Principal Director, Launch Vehicles Systems Engineering. LtCol Dennis Lileikis was the project officer for the program.

This report has been reviewed by the Public Affairs Office (PAS) and is releasable to the National Technical Information Service (NTIS). At NTIS, it will be available to the general public, including foreign nationals.

This technical report has been reviewed and is approved for publication. Publication of this report does not constitute Air Force approval of the report's findings or conclusions. It is published only for the exchange and stimulation of ideas.

LtCol Dennis Lileikis

SMC/CLT

# REPORT DOCUMENTATION PAGE

Form Approved OMB No. 0704-0188

Public reporting burden for this collection of information is estimated to average 1 hour per response, including the time for reviewing instructions, searching existing data sources, gathering and maintaining the data needed, and completing and reviewing this collection of information. Send comments regarding this burden estimate or any other aspect of this collection of information, including suggestions for reducing this burden to Department of Defense, Washington Headquarters Services, Directorate for Information Operations and Reports (0704-0188), 1215 Jefferson Davis Highway, Suite 1204, Arlington, VA 22202-4302. Respondents should be aware that notwithstanding any other provision of law, no person shall be subject to any penalty for failing to comply with a collection of information if it does not display a currently valid OMB control number. PLEASE DO NOT RETURN YOUR FORM TO THE ABOVE ADDRESS.

TO THE ABOVE ADDRESS.				
1. REPORT DATE (DD-MM-YYYY)	2. REPORT TYPE	3. DATES COVERED (From - To)		
01-11-2002				
4. TITLE AND SUBTITLE		5a. CONTRACT NUMBER		
		F04701-00-C-0009		
Burst Testing of Filament-Wound C	Burst Testing of Filament-Wound Graphite-Epoxy Composite Cylindrical Tubes			
		5c. PROGRAM ELEMENT NUMBER		
6. AUTHOR(S)	<u>, , , , , , , , , , , , , , , , , , , </u>	5d. PROJECT NUMBER		
D. J. Chang, H. A. Katzman, J. P. N	lokes, P. M. Adams,			
S. T. Amimoto, P. R. Valenzuela, T	V. V. Albright, P. L. Joseph,	5e. TASK NUMBER		
P. B. Pollock, B. A. Coulter, and J.	P. B. Pollock, B. A. Coulter, and J. K. Ratner			
7. PERFORMING ORGANIZATION NA	ME(S) AND ADDRESS(ES)	8. PERFORMING ORGANIZATION REPORT NUMBER		
The Aerospace Corporation				
Laboratory Operations				
El Segundo, CA 90245-4691		TR-2001(1413)-3		
9. SPONSORING / MONITORING AGE	NCY NAME(S) AND ADDRESS(ES)	10. SPONSOR/MONITOR'S ACRONYM(S)		
Space and Missile Systems Center	1101 1174112(0)7412712511255(25)	SMC		
Air Force Space Command				
-		11. SPONSOR/MONITOR'S REPORT		
2430 E. El Segundo Blvd.	2045	NUMBER(S)		
Los Angeles Air Force Base, CA 90	0245	` '		
		SMC-TR-03-05		
12 DISTRIBUTION/AVAILABIL	ITY STATEMENT			

#### 12. DISTRIBUTION/AVAILABILITY STATEMENT

Approved for public release; distribution unlimited.

## 13. SUPPLEMENTARY NOTES

#### 14. ABSTRACT

An experimental and analytical program was performed to elucidate the failure process of filament-wound graphite-epoxy tubes, especially the effects of wrinkled fibers and of proof testing on tube burst strength. Four types of tubes were tested: those free of flaws, those with a minor or severe helical wrinkle, and those with a hoop wrinkle. Tests included pressurization to burst, and single or multiple proof tests followed by burst. Data collection included burst pressure, acoustic emission events and energies, axial and hoop strains, and location of failure initiation. Tension and torsion tests were performed to determine Young's and shear moduli. Two optical techniques, shadow Moiré and speckle interferometry, were adapted to investigate deformation modes of the tubes. Three types of analysis were performed: composite laminate theory, Weibull analysis of tube strength data, and finite-element analysis of stress distributions near wrinkles. Hoop wrinkles caused an average reduction in burst pressure of 14%; severe helical wrinkles caused an average reduction of 8%. Minor helical wrinkles had no effect. Proof pressures up to ~95% of burst and number of proof testing cycles had no noticeable effect on the average ultimate burst pressures of the tubes.

#### 15. SUBJECT TERMS

Graphite-Epoxy, Filament-Winding, Fracture Behavior, Burst Strength, Wrinkled Fibers, Proof Testing, Acoustic Emission, Shadow Moiré, Speckle Interferometry, Weibull Analysis, Finite Element Analysis

16. SECURITY CLASSIFICATION OF:		17. LIMITATION OF ABSTRACT	18. NUMBER OF PAGES	19a. NAME OF RESPONSIBLE PERSON Dick Chang	
a. REPORT	b. ABSTRACT	c. THIS PAGE	7	65	19b. TELEPHONE NUMBER (include area code)
UNCLASSIFIED	UNCLASSIFIED	UNCLASSIFIED			(310)336-5808

ii

## **Acknowledgements**

This report is dedicated to the memory of Mr. Leonard Horwitz, who was instrumental in initiating and supporting this program.

This project was funded by the Titan SRMU Program Office at The Aerospace Corporation. Mr. G. Dell Jensen, Director of the Engineering Department of the Vehicle Systems Subdivision in Titan Operations authorized the project. Mr. Leonard Horwitz and Mr. Manfred Buechler of the same department were the technical monitors.

The authors wish to express their appreciation to Mr. Ernest Y. Robinson for performing a statistical analysis of the burst data.

# **Contents**

Exec	cutive	Summary	Χi
1.	Back	ground	1
2.	Obje	ctives	3
3.	Mec	hanical Property Testing	5
	3.1	Specimen Descriptions	5
	3.2	End Fittings	5
	3.3	Test Method	7
	3.4	Data Acquisition	7
	3.5	Strain gages	8
4.	Burs	t Pressure Tests and Results	9
	4.1	Test Matrix	9
	4.2	Burst Test Results	10
		4.2.1 Test Series I	10
		4.2.2 Test Series II	11
		4.2.3 Test Series III	15
		4.2.4 Test Series IV	18
	4.3	Discussion	22
	4.4	Mechanical Properties of 2-in. ID Tubes	23
5.	Aco	ustic Emission Measurements	25
	5.1	Acoustic Emission	25
	5.2	Acoustic Monitoring of Tube Tests	25
	5.3	Conclusions	28
6.	Mod	eling and Analysis	31
	6.1	Introduction	31
	6.2	Laminate Analysis of the 2-In, and 4-in. Tube Data	31

	6.3	Weibull Analysis of the Strength Data for Unwrinkled Tubes	35
	6.4	Finite-Element Analysis of Tubes with Wrinkles	38
		6.4.1 Introduction	38
		6.4.2 Wrinkle Modeling	38
		6.4.3 Analysis Results for Helical Wrinkle in 12-Ply Tube	40
		6.4.4 Helical Wrinkle Analysis Parametric Studies and Results	44
		6.4.5 Analysis Results for Hoop Wrinkle in 9-Ply Tube	45
		6.4.6 Hoop Wrinkle Analysis Parametric Studies and Results	48
	6.5	Conclusions of Modeling Efforts for Wrinkles	48
7.	Opti	cal Diagnostic Methodologies	51
	7.1	Shadow Moire	51
	7.2	Speckle Interferometry	52
	7.3	Sample Preparation	53
	7.4	Results	53
		7.4.1 Shadow Moiré Results	53
		7.4.2 One-Dimensional Speckle Interferometry Results	54
	7.5	Improvements to Speckle Interferometry of Composite Tubes	57
		7.5.1 The 3-D Speckle System	57
		7.5.2 Phase Measurement and Phase Stepping	60
		7.5.3 Status of Speckle Interferometry Upgrades	60
		7.5.4 Conclusion of Speckle Interferometry Upgrades	61
	7.6	Conclusions	61
8.	Obse	ervations/Conclusions and Summary	63
Refe	rences		65

# **Figures**

3.1.	Cross-section sketch of end fitting.	6
3.2.	Outside view of tube specimen with end fitting.	7
4.1.	Bar charts showing the ratios of proof and burst test pressures for Test Series I	11
4.2.	Longitudinal failure mode and subtracted images showing the failure for test I- 9 (at 13500 fps).	12
4.3	Slanted failure mode and subtracted images showing the failure sequence for test I-8 (at 13500 fps).	12
4.4.	Cross-sectional view at wrinkle of a helically wrinkled tube	13
4.5.	Bar charts showing proof and burst test ratios for Test Series II	14
4.6.	Pressure-time history for Specimen II-6.	14
4.7.	Pressure-time history for Specimen II-5.	15
4.8.	Cross section view at wrinkle of a hoop wrinkled tube	16
4.9.	Bar charts showing the ratios of proof and burst test pressures for Test Series III	17
4.10.	Failure mode and subtracted images showing the failure sequence of Test III-7 (at 13500 fps).	17
4.11.	Sketch showing the tube specimen configuration and wrinkle locations	18
4.12.	Typical cross section of a helical wrinkle for Tube IV	19
4.13.	Bar charts showing proof and burst test ratios for Test Series IV	20
4. 14.	Failure mode and subtracted images showing the failure sequence of Test IV-1 (at 13500 fps).	20
4. 15.	Failure mode and subtracted images showing the failure sequence of Test IV-2 (at 13500 fps).	21
4.16.	Failure mode and subtracted images showing the failure sequence of Test IV-5 (at 13500 frames/s).	21
4.17.	Burst pressures for all flaw-free specimens from Test Series I, II, and III	22
4.18	Effects of wrinkles on burst pressure with no proof pressure	23

4.19.	Uni-axial stress-strain for 2-inID graphite-epoxy specimen	24
4.20.	Shear stress-strain curve for 2-inID graphite-epoxy specimen	24
5.1.	Example of a calibration AE event.	25
5.2.	Digital Wave type B-1025 acoustic emission transducer	26
5.3.	Location of the six AE sensors on the composite tube	26
5.4.	Acoustic emission recorded while pressure cycling Tube # 11-6.	28
5.5.	Comparison of the AE energy between a tube with a minor helical wrinkle and one with a hoop wrinkle.	29
6.1.	Burst data for tubes w/o wrinkles	36
6.2.	Weibull Plots for burst strengths of tubes	37
6.3.	Finite-element model of tube with helical wrinkle.	39
6.4.	Finite-element model of 9-ply composite tube with hoop wrinkles	40
6.5.	Predicted hoop strains in 12-ply tube with a helical wrinkle (Series IV)	41
6.6.	Predicted helical strains in 12-ply tube with a helical wrinkle	42
6.7.	Predicted interlaminar shear stresses in 12-ply tube with a helical wrinkle	42
6.8.	Outer surface hoop strains in 12-ply tube with a helical wrinkle, scaled to 7675 psi internal pressure	43
6.9.	Outer surface axial strains in 12-ply tube with a helical wrinkle, scaled to 7675 psi internal pressure	44
6.10	Predicted hoop fiber strains for hoop wrinkled tube ran at 2716 psi.	45
6.11	Predicted interlaminar shear stresses for hoop wrinkled tube ran at 2716 psi	46
6.12.	Displacement results with 15% magnification	47
6.13.	Outer surface hoop strains in 9-ply tube with hoop wrinkles	48
7.1.	A cylindrically curved grating with grating lines perpendicular to the cylinder axis is placed in close contact with the surface of the cylindrical tube.	51
7.2.	Schematic for speckle interferometry	52
7.3.	Cross section of 4-in. tube with hoop wrinkle	53
7.4.	Moiré image of size 2.8 in. (v) and 8 in. (h)	55

7.5.	Speckle images centered on defect	56
7.6.	Backside of tube opposite the hoop defect	56
7.7.	Geometry of speckle scattering.	58
7.8.	Two projections of the geometry of 3-D speckle tube and camera imaging locations	59
7.9.	The phase of an empty graphite epoxy tube deformed by placing a wrench into the center of the tube	61
	Tables	
4.1.	Description of Wrinkle Types and Locations	9
4.2.	Burst Test Conditions	9
4.3.	Results for Test Series I	10
4.4.	Results for Test Series II	13
4.5.	Results of Test Series III	16
4.6.	Results of Test Series IV	19
5.1.	Listing of burst tests monitored for AE	27
6.1.	Fiber and Ply Data for the 2-In. Tubes	32
6.2.	Ply Input Properties for Laminate Analysis	32
6.3	Test Data and Predictions for 2-In. Tubes	33
6.4.	Calculated Ply Stresses in Series-I,II,III Tubes (4.0 in Diameter, 9-ply) Loaded to 2860 psi Internal Pressure	34
6.5	Calculated Ply Stresses in Series-IV Tube (4.0 in Diameter, 12-ply) Loaded to 7675 psi Internal Pressure	34
6.6.	Burst Strengths of Unwrinkled Tubes.	34

## **Executive Summary**

This report describes an experimental and analytical program to elucidate the failure process of filament-wound graphite-epoxy tubes, especially the effects of wrinkled fibers and of proof testing on tube burst strength.

Four 11-ft-long graphite-epoxy composite tubes were filament-wound with Toho G30-500-12K fibers in Epon 828 epoxy resin. Each one of the four was manufactured with a unique feature. The first three were manufactured with a lay-up of 9 plies with wind angles with regards to the axial direction of (+10°, -10°, 90°)<sub>3</sub>, (six 10° helical layers and three hoop layers). The inner diameter of each tube was 4.0 in., and the wall thickness was 0.072 in. The fourth tube had a layup of (+15°, -15°, 90°, 90°)<sub>3</sub> for a total of 12 plies (six 15° helical layers and 6 hoop layers). The inner diameter of the fourth tube was also 4 in., with a wall thickness of 0.096 in. The composite tubes were cut into 15-in. lengths that were subjected to internal hydraulic pressure, thereby creating a biaxial stress state in the tube walls. During pressurization of specimens from the first three tubes, the hoop fibers were subjected to stresses nearly four times those of the helical fibers. In samples from the fourth tube, the hoop fiber stress was nearly twice that of the helical fiber stress. Since these tubes do not have inner insulation to prevent water leakage during hydraulic testing, an internal rubber bladder was used so that the pressure could be maintained at a constant level. Acoustic transducers were mounted on the tube surface of some specimens to detect any fiber breakage or delaminations during pressure holds, pressure cycling, or rupture. Rosette strain gauges in 0°, 45°, and 90° orientations were attached to the surface of each tube, and speckle interferometry was used on some samples to measure local deformations during pressurization. Each experiment was filmed with a high-speed camera to determine the location of fracture initiation and to observe the burst dynamics. Data collection included (1) pressure vs. time, (2) burst pressure, (3) number of acoustic emission events and energies vs. time. (4) axial and hoop strain vs. time, and (5) location of failure initiation.

The four types of tubes studied included: those fabricated as free of flaws as possible, those with a minor wrinkle in one helical layer, those fabricated with a wrinkle in one hoop layer, and those fabricated with a more severe wrinkle in one helical layer. All as-received tubes underwent ultrasonic inspection to ensure that no delaminations or other unintended flaws were present before testing. Test conditions included pressurization directly to burst, single proof tests followed by burst, and multiple proof tests followed by burst. Some of the tubes were proof tested to levels as high as 97% of the average burst pressure, and some were proof tested as many as seven times before bursting. The average burst pressure of 11 flaw-free tubes (9-ply construction) was 2867 psi with a standard deviation of 137 psi. The 6 tubes with the minor helical wrinkle had an average burst pressure of 3022 psi with a standard deviation of 109 psi. The tubes with hoop wrinkles had an average burst pressure of 2475 psi with a standard deviation of 271 psi. Therefore, the average strength degradation due to the hoop wrinkles was about 14%. Since the fourth tube had twice as many hoop fibers, the baseline burst pressure for unwrinkled samples was 7652 psi, with a standard deviation of 32 psi. The samples from this tube with a severe helical wrinkle burst at an average of 7077 psi, with a standard deviation

of 219 psi. Therefore, the average strength degradation due to the severe helical wrinkle was about 8%.

In order to analyze these tubes to model and predict the effects of the wrinkles, tension, and torsion tests to determine Young's and shear modulus data were performed on 2-in.-ID tubes of material and lay-up similar to the 9-ply 4-in. tubes.

Three types of analysis were performed: (1) behavior of 2-in. and 4-in. tubes using composite laminate theory, (2) Weibull analysis of tube strength data, and (3) finite-element analysis of stress distributions near hoop and helical wrinkles.

Two non-contacting optical diagnostic techniques were adapted to investigate the deformation modes of the tubes: shadow Moiré and speckle interferometry. These are designed to measure, respectively, the out-of-plane and in-plane deformations during tube pressurization.

Although we did not do a statistically significant number of experiments, there are two strong trends in the data that are worthy of mention:

- 1. Proof pressures up to ~95% of burst and number of proof testing cycles had no noticeable effect on the average ultimate burst pressures of the tubes. With only one exception, all of the tubes burst at a higher pressure than the proof pressures applied. The lone sample that failed at a lower pressure was proofed three times to 98% of the average burst pressure and failed at a pressure about 0.2% lower than the pressure applied for the three prior proof cycles.
- 2. The burst strengths of the tubes with no wrinkles that were studied in this program were designed to be dominated by the hoop fibers. For these tubes, minor helical wrinkles had no measurable effect on the burst pressure. More severe helical wrinkles caused an average reduction in burst pressure of 8%. Hoop wrinkles caused a significant degradation in strength (14% on average).

#### Some other observations:

- All of the tubes, with one exception, failed as the pressure level was increasing. One tube
  failed 5 s into a hold cycle. There was no significant acoustic activity detected during
  this hold.
- The failure initiation points were determined by examining the high-speed camera images. In the tubes with wrinkles, all failures initiated in the immediate vicinity of the wrinkles. All the failures occurred either in the membrane area (no defects) or in the vicinity of the fabricated defects. No effects from the end fittings were observed.
- Acoustic emission data showed no large-energy events that corresponded to delaminations or fiber breaks during pressure holds. However, many low-energy events

corresponding to growth of microcracks at the microscale level were recorded during initial pressurization. All of the tubes were quiet when re-pressurized to equivalent pressures.

- Acoustic emission monitoring provided an excellent method for discriminating between
  tubes with a nominal burst pressure and those that burst at low pressure. The tubes that
  burst low (i.e., tubes with hoop wrinkles) exhibited more higher-energy events at low
  pressures than their nominal counterparts.
- Linear finite-element analyses of the tubes with wrinkles produced mixed results. On the one hand, analysis of the tubes with severe helical wrinkles produced quite good agreement with experiments. The measured drop in burst strength was roughly 8%, while the predicted drop was 12%. However, the finite-element analysis of the tubes with hoop wrinkles overestimated the strength reduction due to fiber misalignment.
- Shadow Moiré identified the role of known hoop defects leading to rupture. In addition, unusual flexing of the tube surfaces during low-pressure inflation was noted. This indicates that local shape changes take place well below the burst limit, especially in areas associated with defects. These deformations were also observed using speckle interferometry. These two optical diagnostic techniques hold promise for identifying potential critical defects in a tube well below its burst limit, and could lead to new techniques for the identification of critical defects during the proof testing of composite pressure vessels.

It is not clear whether the growth of microcracks at low pressures seen in the acoustic emission, shadow Moiré, and speckle interferometry data is significant. Also unknown is whether it is beneficial or detrimental to the ultimate tube strength. These microcracks might weaken the tubes sufficiently to cause lower burst pressures. Alternatively, they might blunt the stress concentrations within the composite and somewhat mitigate the effect of the fiber wrinkles. More work is required to better understand this phenomenon.

# 1. Background

The current level of understanding of structural strength degradation of graphite-epoxy rocket motor cases caused by localized defects is limited, making it difficult to quantify the effects of fiber wrinkles on burst strength. Also unknown is whether hydroproof testing could degrade the strength of graphite-epoxy motor cases, and whether cases could subsequently fail at a service pressure below the proof pressure.

This report describes an experimental and analytical program to elucidate the failure process of filament-wound graphite-epoxy tubes, especially the effects of wrinkled fibers and of proof testing on tube burst strength.

## 2. Objectives

The objectives of this program are:

- to elucidate the burst failure behavior of filament-wound graphite-epoxy tubes, especially the effects of wrinkled fibers and of proof testing on burst strength,
- to gain useful data on whether a composite with or without wrinkles can survive
  a reproof test, especially when the proof pressure is very close to the failure
  strength of the composite,
- to determine how best to utilize diagnostic data during proof and reproof,
- to collect acoustic data during pressurization to correlate with composite behavior,
- to generate pertinent mechanical property data required for modeling and analyses, and
- to understand how the tubes deform during pressurization with the goal of identifying potential critical defects below burst pressures.

## 3. Mechanical Property Testing

## 3.1 Specimen Descriptions

This program included four series of tests. The first series was conducted using filament-wound graphite-epoxy tubes with no known defects to establish the baseline burst pressure. These tubes had a 4.0-in. ID and a lay-up pattern of  $(+10^{\circ}, -10^{\circ}, 90^{\circ})_3$ . In the second and third test series, helical and hoop wrinkles, respectively, were wound into the tubes. The fourth tube had a lay-up of  $(+15^{\circ}, -15^{\circ}, 90^{\circ}, 90^{\circ})_3$  giving a total of 12 plies. A much more severe helical wrinkle than that of the second test series was wound into the tubes. Details of the wrinkle configurations are described in the following sections.

One 2.0-in.-ID tube with a lay-up identical to the first three tubes was also fabricated. This tube was tested under uni-axial tension and torsion to generate uni-axial tensile and shear modulus values for inputs to the analyses.

The burst test specimens were filament-wound graphite-epoxy thin-wall tubes. The tubes were made of Toho G30-500 12K graphite filaments in epoxy resin Epon 828. All tubes had a nominal inner diameter (ID) of 4.0 in. Tubes for the first three test series had a nominal wall thickness of 0.072 in. and an estimated fiber volume fraction of 65%. Since the tubes of the fourth series had 12 plies, their wall thickness increased to 0.096 in. Each tube was fabricated with an overall length of 11 ft (132 in.). The length of the tube specimen tested was typically 15.0 in. Two 6-in.-long end pieces were discarded to eliminate edge effects. A special end cap was designed and fabricated for the tubes. These end caps adhered directly to the tubes, allowing the tubes themselves to carry the axial load as well as the radial load induced by the internal pressure.

The mechanical properties of typical Toho G30-500 graphite filaments and Epon resin system are listed below:

	Ultimate Tensile Stre Tensile Modulus (psi) (psi)		ength Strain-to-Failure (%)	
Toho Filament	34 x 10 <sup>6</sup>	550 x 10 <sup>3</sup>	1.6	
Epon 828 Resin	0.415 x 10 <sup>6</sup>	17 x 10 <sup>3</sup>	10.6	

The tube specimens were fabricated using a filament winding technique by Advanced Composite Products & Technology (ACPT), Inc., Huntington Beach, CA.

### 3.2 End Fittings

A problem associated with realistic pressure testing of cylindrical specimens is that the tube ends must be sealed in such a manner that (1) the tube doesn't leak, (2) that there is no significant amount

of bending stress at the interface between the tube and the end fitting, and (3) that the axial load of the internal pressure is carried entirely by the cylindrical walls of the tube. In typical designs, a metal flange with an insert is utilized to bond the tube specimens using adhesive. The adhesive is under shear stress when the tube is internally pressurized. The shear strength of the adhesive depends upon the type of adhesive used, the bonding procedure, the material for the adherent, and the cure operation. However, regardless of how carefully the bonding operation is conducted, the failure of a cylindrical composite tube under internal pressure often occurs at the end fitting/tube interface.

The end fittings used for this program are an improved version of those designed and used for earlier The basic concept is to apply a radial compression to the end fitting insert/tube intertesting. face. This compression generates a mechanical friction force (or shear force) when the tube and the end fitting are being pulled apart longitudinally. This increases the shear strength capability of the end fitting by an amount equal to the product of the compressive stress, the friction coefficient, and the contact area between the tube and the insert. Figure 3.1 shows the design of the end fitting used to generate the radial compression. The fixture includes a circular flange plate with an inner insert, a ferrule, and a retainer plate with an outer diameter equal to that of the flange. The ferrule has a tapered thickness such that it is thicker toward the base and thinner at the tip. The thin section at the tip gives high radial compliance to limit stress concentrations between the ferrule and the tube that may induce early failure. The retainer plate has an inner diameter slightly smaller than the outside diameter of the ferrule so they interfere. Both the flange and the retainer plates have 16 holes aligned at the same radial and angular locations. In assembling the fitting, the inner surface of the tube is first bonded to the outer surface of the inner insert. The outer surface of the tube is then bonded to the inner surface of the ferrule. The interference between the retainer plate and the ferrule introduces a gap between the retainer plate and the flange. These two components are then forced to contact by tightening the 16 bolts through the holes. This procedure brings the ferrule, the tube, and the inner insert in radial compression. The radial compression increases the shear strength between the tube and the end fitting by an amount equal to  $\mu NA$  where  $\mu$  is the frictional coefficient, N is the normal compressive stress, and A the total contact area between the tube and the ferrule and between the tube and the inner insert. The estimated values of  $\mu$ , N, and A are:  $\mu = 0.25$  to 0.4; N = 8000 psi; and A = 25.0 in<sup>2</sup>. These give allowable internal pressures between 4000 and 6300 psi. The adhesive between the epoxy and the stainless steel has a shear strength of 4000 psi. A combination of the shear strength from compression-induced friction and the adhesive bonding gives the necessary shear-load-carrying capability to the tube/end fitting assembly against end fitting slippage. This design operated flawlessly at pressures of nearly 8000 psi in our testing. Figure 3.2 depicts a specimen with end fittings assembled.

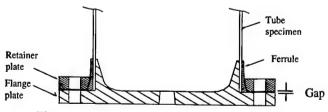


Figure 3.1. Cross-section sketch of end fitting.

## 3.3 Test Method

The basic test procedure involved hydraulically pressurizing the test sample to failure. A Buna rubber bladder was first inserted inside the specimen before the second end cap was bonded. The rubber

bladder was then filled with ethylene glycol. Ethylene glycol was used instead of water to prevent corrosion of the accumulator piston that was used to transfer the gas pressure.

For safety reasons, the testing was conducted inside a 46-in. cubic box made from 1-in.-thick Lexan material. The maximum expected pressures for rupturing the specimens were estimated to be between 3000 to 3500 psig for the first three test series specimens and 6000 to 7000 psig for the fourth test series specimens. The high-pressure source was either a 6000 psi dry nitrogen bottle or a 10,000 psi gas accumulator. All plumbing used 3/16-in.-dia stainless-steel tubing.

## 3.4 Data Acquisition

The primary data acquired for these test series included pressure-time histories and video images. The pressure-time histories were acquired using two Endevco model 8511A pressure transducers with a ranges of 0 to 5000 psig and 0 to 10,000 psig. The data were recorded using a 12-bit A-to-D converter card and LabView software. Data were typically recorded at 50 to 100 points/s. Calibration factors provided by the transducer manufacturer were used to convert the recorded voltages into pressure values.

Video images were acquired both with a standard (30-Hz) frame rate camera, and with a Kodak High-Speed Motion Analyzer Model 4540. This camera is capable of operating at frame rates up to 40,500 frames per second (fps), and has a video array of 256 x 256 pixels. When the camera speed is set at 4500 fps or less, the entire array is scanned to receive images. At 13,500 and 18,000 fps the array sizes are 128 x 128 and 256 x 64, respectively. The High-Speed Motion Analyzer has sufficient memory to store 1024 full size images (256 pixels in both directions). At 4500 fps, it can record an event of 0.227 s duration. At 18,000 fps, the number of recorded frames increases to 4096, and the duration of a recorded event remains at 0.227 s. We chose either 18,000 or 13,500 fps for recording this test series. At 18,000 fps speed, the image captures 256 pixels in the horizontal direction and 64 pixels in the vertical direction. At 13,500 fps speed, the images can include the images from a mirror reflecting the back surface of the specimen. This view covered the entire tube specimen with reasonable resolution.



Figure 3.2. Outside view of tube specimen with end fitting.

The high-speed camera was triggered using a copper wire wound around the surface of the tube from one end to other. When the specimen burst, it broke the wire, causing a trigger signal to be sent to the camera. While waiting for the trigger signal, the camera would continuously record images, cycling through its memory. When the trigger signal was received, the camera would save the last half of the images currently in memory, and continue recording long enough to refill the other half of the memory. The net result is a collection of sequential images centered on the trigger point. When operating at either 18,000 or 13,500 fps, the camera produces 2048 pre-trigger frames and 2048 post-trigger frames.

## 3.5 Strain gages

Rosette type strain gages were mounted on several tubes to collect pressure vs. strain data during testing. Uni-axial tension and torsion tests were also conducted with the same type of rosette gages mounted for modulus determination.

## 4. Burst Pressure Tests and Results

#### 4.1 Test Matrix

Three 11-ft-long graphite-epoxy tubes of lay-up  $(+10^{\circ}, -10^{\circ}, 90^{\circ})$  were procured with different wrinkle conditions. The first tube had no wrinkle; the second tube had helical wrinkles fabricated in part of the tube; and the third had hoop wrinkles fabricated in part of the tube. The fourth tube of lay-up  $(+15^{\circ}, -15^{\circ}, 90^{\circ}, 90^{\circ})$  had a more severe helical wrinkle than the second tube. All as-received tubes underwent ultrasonic inspection to ensure that no delaminations or other unintended flaws were present before testing. The type and number of 15-in. segments with wrinkles for each tube are listed in Table 4.1.

A total of 28 successful burst tests were conducted. Several preliminary tests were conducted to identify the best rubber bladder configuration. Some tubes were pressurized directly to burst, and others were first proof tested at different percentages of the "average" burst pressure followed by a burst test. Table 4.2 shows the test conditions for all specimens.

Table 4.1. Description of Wrinkle Types and Locations

Type ID and Type of Wrinkle	Total number of tube segments	No. of segments with wrinkles	Remarks
Tube 1 No Wrinkles	9	0	NA
Tube 2 Minor Helical Wrinkles	8	7	One wrinkled tube was used for microstructural examination
Tube 3 Hoop Wrinkles	8	6	One wrinkled tube was used for microstructural examination
Tube 4 Severe Helical Wrinkles	8	6	A 2-inwide strip fabricated with a wrinkle was used for microstructural examination

Table 4.2. Burst Test Conditions

Test No.	Series I No wrinkle	Series II Minor helical wrinkle	Series III Hoop wrinkle	Series IV Severe helical wrinkle
1	Straight burst	No wrinkle Straight burst	No wrinkle Straight burst	No wrinkle Straight burst
2	Straight burst	Straight burst	Straight burst	Five proofs at various pressure levels followed by burst
3	One proof followed	Straight burst	One proof followed by burst	No wrinkle
	by burst			Straight burst
4	One proof followed by burst	Six proofs followed by burst	No wrinkle Straight burst	One 5 min proof followed by burst
5	One proof followed by burst	Three proofs followed by burst	One proof followed by burst	Four proofs at various pressure levels followed by burst
Te	st Series I	Series II	Series III	Series IV

No.	No wrinkle	Minor helical wrinkle	Hoop wrinkle	Severe helical wrinkle
6	One proof followed by burst	Six proofs followed by burst	Six proofs followed by burst	For optical diagnostic measurements
7	Straight burst	Straight burst Four proofs at variou pressure levels followed by burst		s Un-tested
8	One proof followed by burst	Used for microstructure examination	Used for micro- structure examination and speckle interferometry	Un-tested
9	Straight burst	NA	NA	NA

## 4.2 Burst Test Results

### 4.2.1 Test Series I

A total of nine 15-in. specimens were cut from the 11-ft-long tube and tested for this group. Three tubes were tested for establishing the baseline burst pressure. The average burst pressure was 2860 psi. Six tubes were planned for a single proof test before bursting. The ratio of proof pressure to the average burst pressure varied from 0.88 to 0.97. The results of the Test Series I are shown in Table 4.3. Figure 4.1 depicts a bar chart showing the ratios of proof and burst pressures to the average burst pressure for Series I. Specimen No. 9 was intended to be proof tested at 97% of the average burst strength, but failed 5 s into the proof pressure hold. This result implies that a time-delayed failure can occur. Time-delayed failure of graphite-epoxy composite structures is not well understood and requires further study.

The data from this series do not suggest that proof pressure testing reduces the ultimate burst pressure. Proof pressure testing at pressures below 96% of the average burst pressure does not appear to degrade the strength of the tubes.

Table 4.3. Results for Test Series I

Specimen ID	Proof Test Pressure (psi)	Burst Test Pressure (psi)	Proof Pressure/Ave. Burst Pressure	Burst Pressure/Ave. Burst Pressure	Remarks
I-1	Not proof tested	2861		1.00	
I-2	Not proof tested	2850		0.994	An average of 2860 psi is obtained from Tests I-1, I-2, and I-7.
1-3	2533	2665	0.884	0.932	Air bubbles may have entered the specimen on refilling.
1-4	2596	2768	0.91	0.965	
I-5	2673	2698	0.932	0.941	
1-6	2760	2997	0.963	1.05	High burst pressure after proof.
1-7	Not proof tested	2869		1.00	<u> </u>
1-8	2742	3054	0.96	1.045	High burst pressure after proof.
I-9		2787		0.972	Failed at end of proof pressurization (5 s delayed failure).

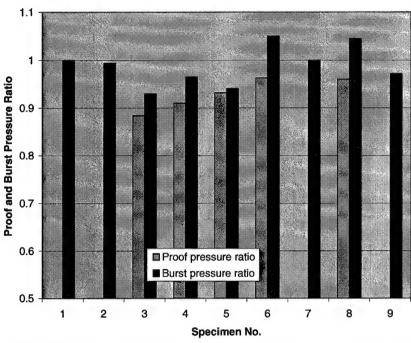


Figure 4.1. Bar charts showing the ratios of proof and burst test pressures for Test Series I. (Average burst pressure of baseline tubes is 2860 psi.)

There are typically two fracture modes for Series I. Figures 4.2 and 4.3 depict the two types of failures as well as the subtracted frames from their respective reference frame at 74-µs time intervals. One was a longitudinal mode with a crack running primarily in the axial direction as seen in Figure 4.2. In this figure, frame -89 was the last frame before bursting. In frames -88 and -87, the fracture line is visible in the lower part of the tube. The two photographs in the second row are the subtracted images of frames -88 and -87 from unfractured reference frame -89. There was, however, a small curvature at the center portion of the tube that became large when approaching the end fitting. The large angle at the ends may be the effect of fixed boundary conditions.

The second type of failure mode was a slanted crack at about 45° from the axial direction, as depicted in Figure 4.3. Frame –85 was the last frame before bursting and serves as the reference frame. Similar to Figure 4.2, the two dark photographs in the second row of Figure 4.3 correspond to the subtracted images in reference to frame –85. In this mode, the fracture ran in the 45° direction and extended through the rest of the tube.

In Figures 4.2 and 4.3, there are two tube images in each frame. This is because a mirror was installed to reflect the image of the back surface of the specimen so that the fracture initiation would be captured if the fracture initiated from the back surface.

## 4.2.2 Test Series II

In this test series, seven 15-in.-long segments with helical wrinkles and one 15-in.-long segment with no wrinkle were cut from an 11-ft-long tube. The fiber lay-up angles in the tube were the same as

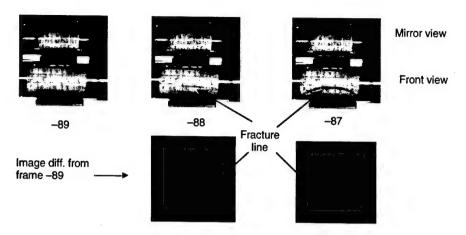


Figure 4.2. Longitudinal failure mode and subtracted images showing the failure for test I- 9 (at 13500 fps).

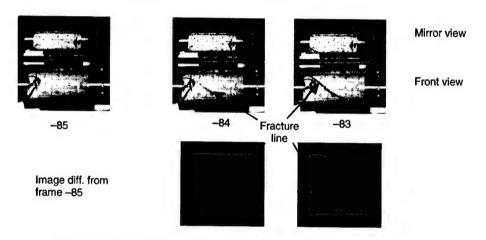


Figure 4.3 Slanted failure mode and subtracted images showing the failure sequence for test I-8 (at 13500 fps).

those in the Test Series I tube. The burst pressure value from the un-wrinkled segment served as the baseline. The helical wrinkles were created using partially cured circular resin rings. The rings were circumferencially placed at designated locations 15 in. apart during the winding operation. Figure 4.4 depicts the cross section of a helically wrinkled tube. Due to the fact that the resin ring was only partially cured before winding, it was relatively soft. The radial pressure from the winding process flattened the ring, causing its height to be reduced from 0.04 in. to about 0.02 in. The hoop layer under the ring was also somewhat compressed.

Since the single proof tests performed in Test Series I did not appear to have any significant effect on the ultimate burst pressure, it was decided to increase the number of proof cycles in Test Series II. It was thought that multiple proof cycles might show strength degradation not seen in single proof tests.

The results of Test Series II are shown in Table 4.4. The average burst pressure was 3005 psi. Figure 4.5 depicts bar charts showing the ratios of proof and burst pressures for Series II. The number

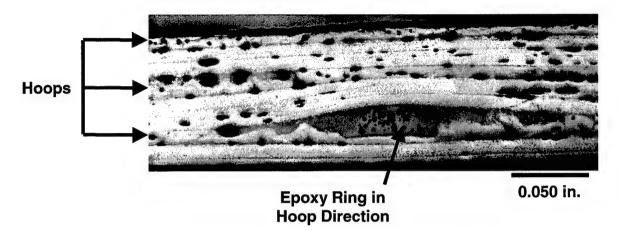


Figure 4.4. Cross-sectional view at wrinkle of a helically wrinkled tube.

Table 4.4. Results for Test Series II

Specimen ID	Proof test pressure (psi)	Burst test pressure (psi)	Proof pressure Average burst	Burst pressure Average burst	Remarks
II-1	Not proof tested	2667		0.888	Specimen with no wrinkle. Baseline test. Low burst pressure compared to others. Two 0/45/90 strain gages mounted. Data taken on 0/90 gages AE data taken.
II-2	Not proof tested	2950		0.98	Specimen had a helical wrinkle. Two 0/45/90 strain gages mounted. Data taken on 0/90 gages. AE data taken.
II-3	Not proof tested	3059		1.018	Specimen had a helical wrinkle. Tubes II-2 and II- 3 used as baseline tests. Avg. 3005 psi.
11-4	2786	3010	0.927	1.002	Specimen had a helical wrinkle. Six proof cycles at average of 2786 psi.
II-5	2966	2959	0.981	0.979	Specimen had a helical wrinkle. Three proof cycles at average of 2930 psi. Failed at end of pressurization of 4 <sup>th</sup> cycle.
II-6	2911	3224	0.969	1.073	Specimen had a helical wrinkle. Six proof cycles at average of 2911 psi.
II-7	Not proof tested	2933		0.976	Specimen had a helical wrinkle. Intended for six proof cycles at 2900 psi. Failed at 2933 psi at end of 1st cycle. No time- delayed failure.

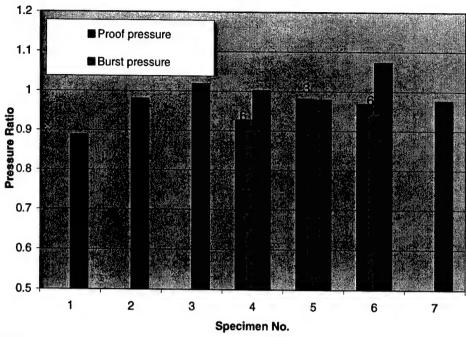


Figure 4.5. Bar charts showing proof and burst test ratios for Test Series II. (Average burst pressure of baseline tubes is 3005 psi.)

above each light-gray bar indicates the number of proof tests conducted for this particular specimen. The burst pressure of the un-wrinkled specimen, II-1, was 2667 psi. This burst pressure was significantly lower than the burst pressure values of the wrinkled segments from the same tube. The fact that this segment was cut from the end of the 11-ft tube might be the cause of the abnormal burst pressure.

The six wrinkled segments were tested in two conditions: three were pressurized directly to burst, and three were proof tested before burst. For each proof cycle, the peak pressure was maintained for 2 min before venting. As seen in Table 4.4, there were no differences in burst pressures between proof-tested and un-proof tested specimens other than typical data scatter for composite materials. A typical pressure-time history plot is depicted in Figure 4.6.

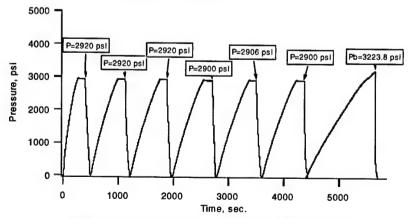


Figure 4.6. Pressure-time history for Specimen II-6.

For specimen II-5, there may be a proof test effect on the strength of the specimen. The specimen was pressurized three times to 98.1% of the average burst pressure. The specimen, however, failed while the proof pressure was reached on the fourth cycle without being able to sustain the 2-min-long hold. This showed that the specimen strength might have been degraded by the previous three proof cycles. Figure 4.7 depicts the pressure-time history of this test.

Specimen II-7 was intended for a six-cycle proof test, but it failed toward the end of the first cycle. The burst pressure was 97.6% of the average burst pressure.

As mentioned earlier, the helical wrinkle did not noticeably degrade the tube strength. One reason is that the strength of the tube is dominated by the hoop fibers. The composite stress in the hoop direction is twice the stress in the axial direction. However, the number of helical fibers is twice that of the hoop fibers. This results in an approximate factor of 4 in the fiber-to-stress ratio in the helical direction as compared to the hoop direction. The reduction of the strength due to a 10° inclination of the helical fibers from the axial direction is small, only a few percent. Although there was some strength degradation to the helical fibers from the helical wrinkles, the degradation was far from enough to cause any helically dominated failure. The failure modes of this series are similar to those observed in Series #1: either a longitudinal fracture mode or an inclined fracture mode.

#### 4.2.3 Test Series III

In this test series, six 15-in.-long segments with hoop wrinkles and two 15-in.-long unwrinkled segments were cut from an 11-ft-long tube. Only 5 of the 6 wrinkled tubes were burst. The fiber lay-up angles in the tube were the same as those in the Test Series I and II tubes. The two unwrinkled segments served as the baseline, and the average burst pressure from the two unwrinkled segments was 2992 psi. The unwrinkled segments were cut from the middle portion of the 11-ft-long tube. The hoop wrinkles were created using two 8-in.-long graphite/epoxy rods fully cured in advance. The two rods ran longitudinally and were symmetrically located in the middle portion of each segment. One rod was below and the other was above the second hoop layer. The wrinkle weakened the load-carrying capability of the tube in the hoop direction. Figure 4.8 depicts a cross-section of a hoop-wrinkled tube.

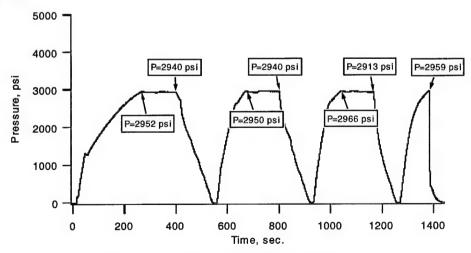


Figure 4.7. Pressure-time history for Specimen II-5.

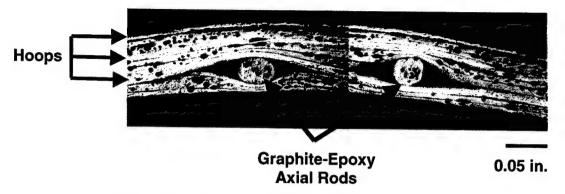


Figure 4.8. Cross section view at wrinkle of a hoop wrinkled tube.

The test results shown in Table 4.5 indicate that a hoop wrinkle significantly reduces the burst pressure. The fabricated hoop wrinkle was much more effective in degrading the strength than the helical wrinkle. The burst pressure was reduced by 10–27% of the pressure for un-wrinkled specimens. Figure 4.9 depicts the bar charts showing the ratios of proof and burst test for this test series. The number "6" corresponding to specimen No. 6 indicates that this tube was proof tested six times before burst. The letter "M" indicates that the specimen III-7 went through 4 multiple proof test cycles as listed in Table 4.5. It should be noted that one tube was cut for microstructural examination so that only seven specimens were available for testing.

Table 4.5. Results of Test Series III

Specimen ID	Proof test pressure (psi)	Burst test pressure (psi)	Proof pressure Average burst	Burst pressure Average burst	Remarks
III-1	Not proof tested	3090		1.033	Specimen with no wrinkle. III-1 and III-4 serve as baseline tests. Avg. burst pressure is 2992 psi.
III-2	Not proof tested	2195		0.734	Specimen had a hoop wrinkle.
111-3	1960	2168	0.655	0.725	Specimen had a hoop wrinkle. Proof tested at ~90% of the burst pressure of III-2.
III-4	Not proof tested	2894		0.967	Specimen had no wrinkle. III-1 and III-4 serve as baseline tests. Avg. burst pressure is 2992 psi. Six strain gages mounted.
III-5	2108	2695	0.705	0.901	Specimen had a hoop wrinkle. Proof tested at ~95% of the burst pressure of III-2.
III-6	2125	2716	0.710	0.908	Specimen had a hoop wrinkle. Proof tested six times at ~96% of the burst pressure of III-2.
III-7	2000, 2150, 2300, 2450	2600	0.701	0.869	Proof tested at different levels starting at 2000 psi.
III-8					Cut for microscopy

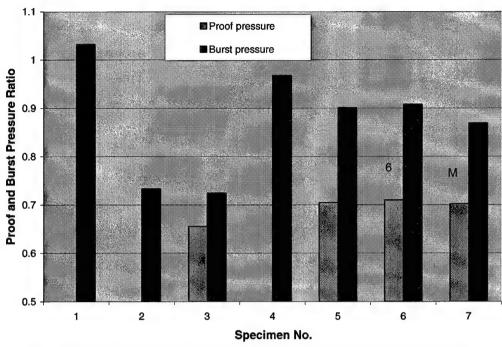


Figure 4.9. Bar charts showing the ratios of proof and burst test pressures for Test Series III. (Average burst pressure of un-wrinkled tube is 2992 psi.)

The failure mode of Test Series III (hoop wrinkles) was different from those observed in Test Series I and #2. Unlike the two failure modes in Figures 4.2 and 4.3, the failure path in these hoop-wrinkled tubes was strongly dominated by the existence of the longitudinal rods. Figure 4.10 depicts the typical failure mode for wrinkled tubes in this series. Frame -64, an un-fractured frame, served as the

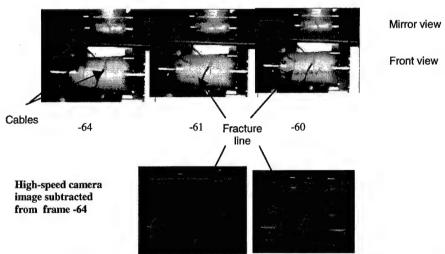


Figure 4.10. Failure mode and subtracted images showing the failure sequence of Test III-7 (at 13500 fps).

reference. The failure initiated at the middle portion of the tube next to the wrinkles, then ran longitudinally parallel to the graphite-epoxy rods. The longitudinal crack at the lower portion of the tube was slightly visible in frame -61 and became very visible in frame -60. This failure mode was observed in all hoop-wrinkled specimens.

#### 4.2.4 Test Series IV

In this test series, eight 15-in.-long segments with severe helical wrinkles were fabricated from an 11-ft-long tube. The fiber lay-up angles in the tube were (±15°, 90°, 90°)<sub>3</sub> with a total of 12 plies. In order to obtain a ring sample for microstructural characterization, one set of the wrinkles was put at the mid point of the entire 132-in.-long tube. This made two 14-in.-long tube specimens (specimens IV-1 and IV-3 in Table 4.6) after a 2-in.-wide ring containing a wrinkle set was machined out. It is believed that a 14-in.-long specimen provides burst pressure information as valid as a 15-in.-long specimen. All other wrinkles were put at the mid point of each tube segment. Figure 4.11 shows a sketch of all wrinkle locations and the tube specimen configuration. The dashed lines represent the wrinkles. The top numbers are length of each segment in inches.

The helical wrinkles were created using three circular resin rings fully cured in advance. Each resin ring had approximately a semi-circular cross section. At each wrinkle location, the first ring was put atop the second 90° layer, and the second and third rings were then put atop the second set of the ±15° helical layer, one on each side of the first ring. Photographs of the microstructure of the wrinkle-ring taken from the middle of the tube and from the post-test specimens indicate that the wrinkles on all specimens were similar. Figure 4.12 depicts a typical cross-section view of the wrinkles. It is seen from Figure 4.12 that the two middle helical layers were S-shape wrinkled by the three resin rings.

The test results shown in Table 4.6 indicate that the helical wrinkles fabricated in this series reduce the burst pressure. The amount of reduction ranges from 6 to 11% based on an average burst pressure of 7653 psi. The embedded resin rings induced localized bending stress to the helical fibers in addition to the pressure-induced membrane stress. Figure 4.13 depicts the bar charts showing the ratios of proof and burst tests for this test series. From Figure 4.13, three data points do not indicate that the proof-pressure ratios (0.78 to 0.85) had any effect on the burst pressure.

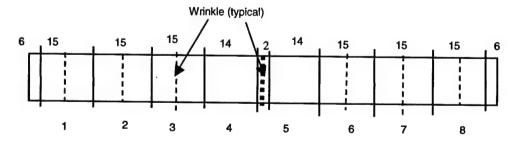


Figure 4.11. Sketch showing the tube specimen configuration and wrinkle locations. The top numbers are length in inches.

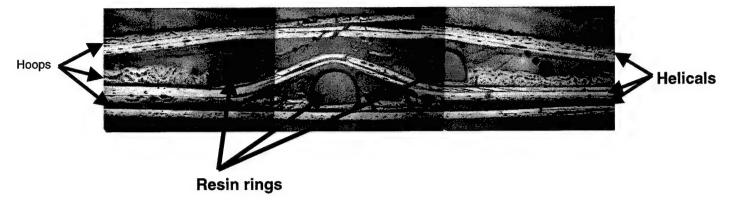


Figure 4.12. Typical cross section of a helical wrinkle for Tube IV. (From post-test piece of Test IV-4.)

Table 4.6. Results of Test Series IV

Specimen ID	Proof test pressure (psi)	Burst test pressure (psi)	Proof pressure (Average burst ratio)	Burst pressure (Average burst ratio)	Remark Specimen with no wrinkle
IV-1	Not proof tested	7630		0.995	Baseline test. No wrinkle. Two 45/90/135 strain gages mounted. AE data taken. High-speed camera imges taken.
IV-2	4500, 5000, 5500, 6000, 6500	7177	0.848	0.936	Specimen had a helical wrinkle. Two 0/45/90 strain gages moounted. AE data taken. Proof ratio 0.59 to 0.85.
IV-3	Not proof tested	7675		1.001	Specimen had no helical wrinkle. No strain gages or AE transducers.
IV-4	6000	7229	0.782	0.943	Specimen had a helical wrinkle. Six strain gages. Six AE tranducers up to proof pressure. UT inspection between proof test and burst test. No HSC images due to low voltage in battery.
IV-5	4300, 5000, 5720, 6440	6827	0.840	0.890	Specimen had a helical wrinkle. Four proof levels at 60%, 70%, 80%, and 90% of avg. burst pressure w/wrinkles (7200 psi). No strain gages. No AE. HSC images caught.

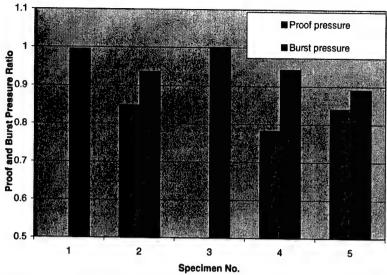


Figure 4.13. Bar charts showing proof and burst test ratios for Test Series IV. (Average burst pressure of un-wrinkled tube is 7653 psi.)

The failure mode of the specimens in this test series is different from those in Series I, II, and III. In the previous three series, the failures were dominated by the hoop fibers with little influence from the helical fibers. This was true because there were half as many fibers in the hoop direction as in the helical direction, while the hoop stress was twice the stress in the axial direction. For this series, the amount of fibers is more or less balanced in both directions. The stress in the helical fibers became more significant at burst pressure, especially in the wrinkle region. Figures 4.14 through 4.16 depict the subtracted images for specimens IV-1, IV-2, and IV-5. Specimen IV-1 had no wrinkle, while specimens IV-2 and IV-5 were wrinkled. From these three figures, it can be seen that the failure for specimen IV-1 was hoop-fiber dominated, the failure of specimen IV-2 was mixed, and the failure of specimen IV-5 was helical-fiber dominated.

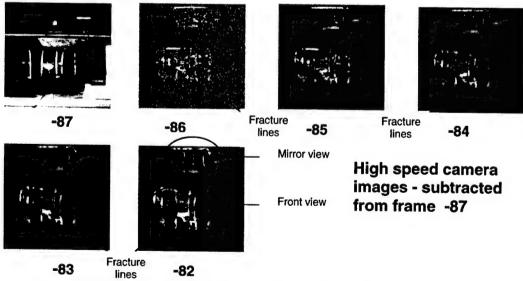


Figure 4. 14. Passure mode and subtracted images showing the failure sequence of Test IV-1 (no wrinkle) (at 13500 fps).

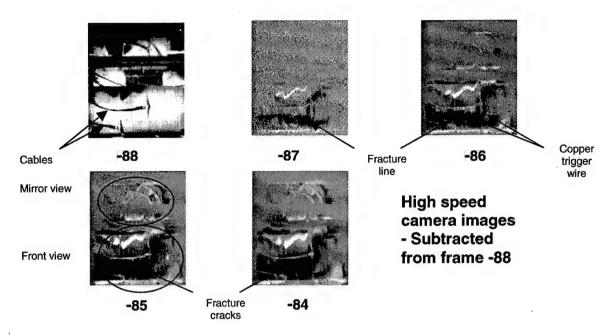


Figure 4. 15. Failure mode and subtracted images showing the failure sequence of Test IV-2 (at 13500 fps).

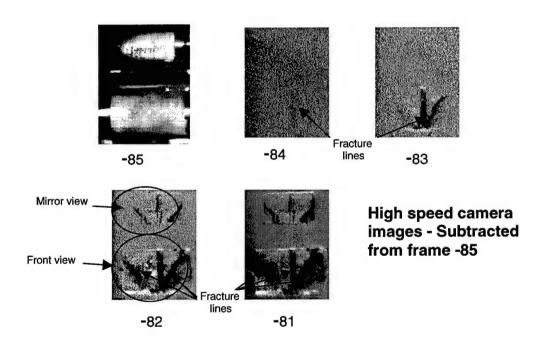


Figure 4.16. Failure mode and subtracted images showing the failure sequence of Test IV-5 (at 13500 frames/s).

In Figure 4.14, AE transducers were mounted to collect the acoustic signals during testing. Frame-87 is the reference frame in which a mirror image of the back surface of the tube and rubber bands holding the AE transducers in place are visible. In frames -86 through -82, the subtracted images of the rubber bands and the fracture line are all visible.

In Figure 4.15, frame -88 is the reference frame. The instrument cables and wire besides the fractured line and crack are all visible in the subtracted images. Similar features of fractures are seen in Figure 4.16,

Similar to the specimens in the Series II and III, rosette strain gages (CEA-06-062UR-350) were mounted on three specimens (IV-1, IV-2, and IV-4). There was one rosette gage on specimen IV-1. The strains in 45/90/135 directions, relative to the axial direction, provided a complete strain field for an unwrinkled specimen. For specimens IV-2 and IV-4, which have wrinkles, two rosette gages (0/45/90) were mounted on each, one on top of the wrinkle and one away from the wrinkle. The data were used for correlating the finite-element modeling analyses that will be discussed in Section 6.

## 4.3 Discussion

The average burst pressure of 11 tested flaw-free tubes from Series I, II, and III was 2860 psi with a standard deviation of 137 psi or 4.8%. Figure 4.17 depicts the burst pressures of these 11 specimens. The 6 tubes with the minor helical wrinkle had an average burst pressure of 3022 psi with a standard deviation of 109 psi or 3.6%. The tubes with hoop wrinkles had an average burst pressure of 2475 psi with a standard deviation of 271 psi or 11.0%. Test conditions included straight burst testing, single proof tests followed by burst, and multiple proof tests followed by burst. Some of the tubes were proof tested to levels as high as 98% of the average burst pressures, and some were cycled to these proof pressures as many as six times before bursting.

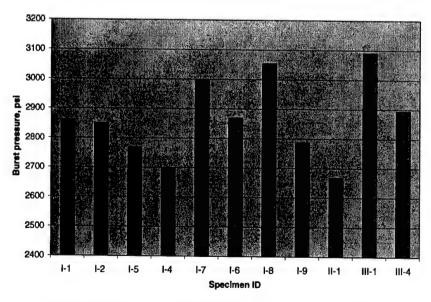


Figure 4.17. Burst pressures for all flaw-free specimens from Test Series I, II, and III.

To show the hoop wrinkle effect, Figure 4.18 was constructed to include all the tube burst data in the same three test series without any proof cycle. The data came from three groups: 5 tubes free from defects, two tubes with helical defects, and a tube with a hoop wrinkle. Figure 4.18 demonstrates that the burst pressures of our helically wrinkled specimens are comparable to those free from defects. The average burst pressure of these seven specimens is 2939 psi. However, the burst strength of the hoop-wrinkled tube falls 25% below the 2939 psi average.

For test series IV, the limited data do not allow any statistical analysis. Since the tubes had different lay-ups from the previous three tubes, the failure pressure values can not be included in the same group. The fiber certification data indicated that the strength and strain-to-failure for the fibers used in winding Series 4 tube were 613 ksi and 1.82%, respectively. However, this fiber strength increase (613/575-1=6.6%) is less than the average burst pressure increase (7653/2867/2-1=33.5%). The factor "2" reflects the ratio of number of hoop plies in Series 4 to that of the earlier series. Other factors such as the increase of helical angle from  $10^{\circ}$  to  $15^{\circ}$  is also a source of the discrepancy.

By examining the microstructural photographs of Test Series IV, it is seen that hoop fiber thinning occurred in the wrinkle area (see Figure 4.12). The hoop fiber thinning may have a strong effect on the strength degradation of the wrinkled tubes. More testing is needed to generate additional strength degradation data for statistical analysis.

### 4.4 Mechanical Properties of 2-in. ID Tubes

Uni-axial tensile testing and torsion tests were conducted using 2-in.-ID tubes that had identical number of layers and lay-up angles as the Series I, II, and III 4-in.-ID tubes. These tests were performed to generate uni-axial stress-strain and shear stress-strain curves for the composite material. The specimens were 12 in. long.

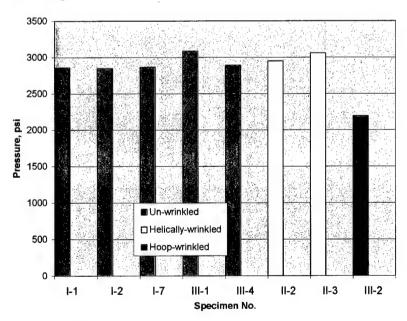


Figure 4.18. Effects of wrinkles on burst pressure with no proof pressure.

The same rosette (0/45/90) type of strain gages (CEA-06-062UR-350) that were used in the 4-in.-ID specimens were mounted on the outside surface of the specimens. There were two gages on each specimen 180° apart at the middle of the specimen, designated as gage 1 and gage 2. For the uniaxial specimen, the 0° and 90° direction gages were parallel to the axial and hoop directions, respectively. In the torsion specimen, they were 45° from the axial and hoop directions in order to record the maximum strain readings. The stress-strain curve for the uni-axial specimen is depicted in Figure 4.19. In Figure 4.19, gage 1 ax, gage 1 45, and gage 1 cir refer to the gage No. 1 in the axial direction, 45° from the axial direction, and circumferential direction, respectively. The same notations apply to gage No. 2. The torsion stress-strain curve is depicted in Figure 4.20. The calculated Young's modulus, E, and the shear modulus, G, are 12.5 msi and 1.10 msi, respectively. The Poisson's ratio (hoop strain to axial strain under axial stress) is 0.13.

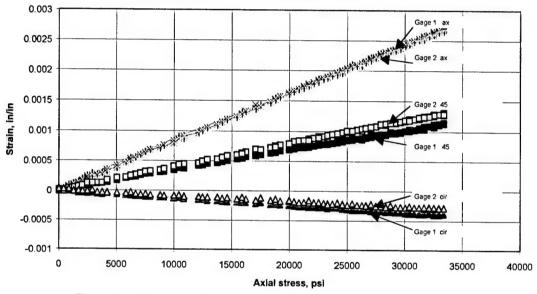


Figure 4.19. Uni-axial strain-stress for 2-in.-ID graphite-epoxy specimen.

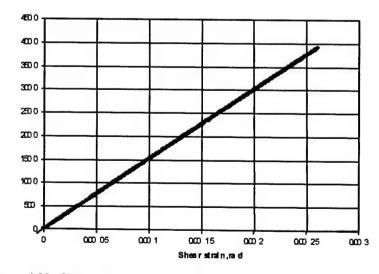


Figure 4.20. Shear stress-strain curve for 2-in.-ID graphite-epoxy specimen.

### 5. Acoustic Emission Measurements

### 5.1 Acoustic Emission

Acoustic emission (AE) monitoring provides a powerful nondestructive evaluation (NDE) technique used to monitor structures during load application. AE is an irreversible energy release generated in a material under stress. In composite structures, AE can be related to a number of fracture mechanisms that include, but are not limited to, matrix cracking, fiber breakage, and delamination. The fracture energy propagates through the material as a stress wave that can be detected and evaluated. Historically, AE testing has been used to locate areas of high stress and predict ultimate failure loads by counting the individual acoustic events that are detected during the load application. The more recent approach to AE monitoring focuses more on the wave characteristics of the acoustic events. Modern systems are designed to record the wave forms associated with the detected acoustic events. Recording the wave information allows for extensive post-test data analysis and review that can provide additional insight into the acoustic properties of materials and a more precise location of damage areas. The downside to wave-based AE systems is their relatively slow data acquisition characteristics. Particularly with composite materials, the slow acquisition rate can result in the system becoming swamped with incoming AE signals. Care must be taken in selecting the system gain to minimize this condition.

## 5.2 Acoustic Monitoring of Tube Tests

A Digital Wave Corporation 6-channel AE system was utilized for the acoustic monitoring of the composite tubes. The Digital Wave instrument consists of pre-amplifiers, signal filters, a triggering system, and a wideband receiver interfaced into a computer. The Digital Wave system records the complete AE signal or "wave" for each detected event. An example of a typical AE signal is provided in Figure 5.1.

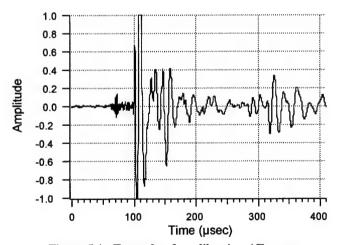


Figure 5.1. Example of a calibration AE event.

An important aspect of any AE system is the type of piezoelectric sensor used to detect the acoustic emission. In this test program, a set of six Digital Wave type B-1025 transducers were used. These sensors are characterized by excellent sensitivity to acoustic activity between 50 kHz and 1 MHz. They are small elements utilizing a micro-dot connector that can easily be held in place with rubber bands looped around the tube. A water-based acoustic coupling gel (Sono-Trace) was used to enhance the acoustic coupling between the transducer and the tubes. An image of the type B-1025 sensor with a quarter dollar for scaling are shown in Figure 5.2.

The risk of damage to the transducers limited the testing of the first series of tubes to only 2 sensors per tube. For Test Series II and III, six sensors were used in the pattern shown in Figure 5-3. A table of the tubes tested with AE sensors is provided in Table 5.1

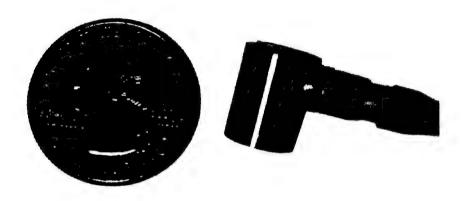


Figure 5.2. Digital Wave type B-1025 acoustic emission transducer.

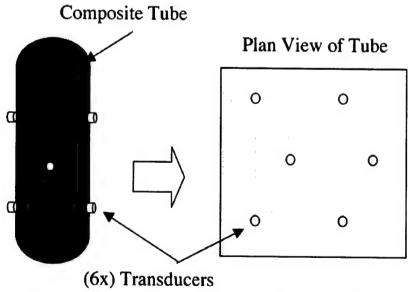


Figure 5.3. Location of the six AE sensors on the composite tube.

Table 5.1. Listing of burst tests monitored for AE

Specimen ID	Number of AE Channels
I-2	2
I-3	2
1-4	2
I-5	2
1-6	2
I-8	2
1-9	2
11-1	6
II-2	6
11-4	6
II-6	6
II-7	6
III-2	6
III-3	6
111-4	6

During the pressurization cycles, a real-time evaluation of the data was performed to determine how the acoustic information could be used to provide an indication of impending failure. Parameters such as rate of event generation, event energy, and amplitude were examined during the pressurization cycles just prior to burst. The acoustic emission in all of the tubes was dominated by matrix microcracking. This is a normal process that is characteristic of all fiber-reinforced composite materials. As the tube approaches the failure load, the matrix is fully cracked, and any subsequent failures occur in the fibers. So one would expect the rate of events/pressure rise to flatten out. This effect was detected in some vessels, but not all. Additional work would be required to develop this acoustic marker into a reliable method for indicating an impending failure in composite tubes.

An important result from this testing was that all of the tubes exhibited the Kaiser effect. The Kaiser effect is the observation that under cyclical loading, undamaged materials will not generate significant additional acoustic emission events until the structure is subjected to a load that exceeds any previous load. This behavior can be used to detect damage that might occur between cycles. An example of the AE signature displaying the Kaiser effect is shown in Figure 5.4. Note that essentially all of the AE occurred during the initial tube pressurization and the final cycle after the pressure had exceeded the previous maximum pressure of ~2975 psi. The small number of events that did occur during the intermediate cycles were caused by noise in the pressurization system.

AE can be used to locate regions of the tubes that are noisier than might be expected. Events are located by measuring the relative arrival time of the AE signals to the different sensors and then triangulating to regions in the tubes. In the case of the hoop-wrinkled tubes, the AE events were concentrated in the same regions that had previously been identified using ultrasound as having significant voids or along the wrinkle insert.

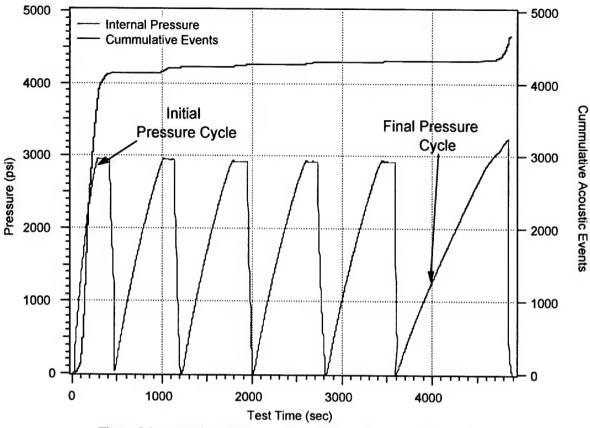


Figure 5.4. Acoustic emission recorded while pressure cycling Tube # II-6.

The AE monitoring did provide an excellent method for discriminating between tubes with a nominal burst pressure and those that burst low. During pressurization, the tubes that burst low (i.e., tubes with hoop wrinkles) had more higher-energy events at low pressures than their nominal counterparts. An example of this is shown in Figure 5.5 for tubes typical of both types. The red traces correspond to pressure (right scale), and the blue traces correspond to acoustic energy (left scale).

## 5.3 Conclusions

Acoustic emission monitoring of the composite tubes indicated that the majority of the events detected prior to burst had characteristics associated with matrix cracking, not delaminations or fiber breakage. This was inferred from the measured energy levels and frequency content in the AE events. Previous work at The Aerospace Corporation has shown that as flaws in the composite grow there are an increasing number of higher energy events that are characterized by large amplitudes and lower frequency than matrix cracking. The test data indicated that the largest energy events tended to occur at pressures of less then 50% of the ultimate burst. It is theorized that the large energies noted at the lower pressures were a localized effect caused by the growth of microcracks in the wrinkled region. It is possible that the microcracks were due to tube circularization, which is discussed in Section 6.3. In this application, the AE data provided a tube quality indication based on the overall number of significant AE events and the onset pressure. This was dramatically illustrated in a comparison of the AE data obtained from helical-wrinkled tubes with burst pressures above 3000 psi and the

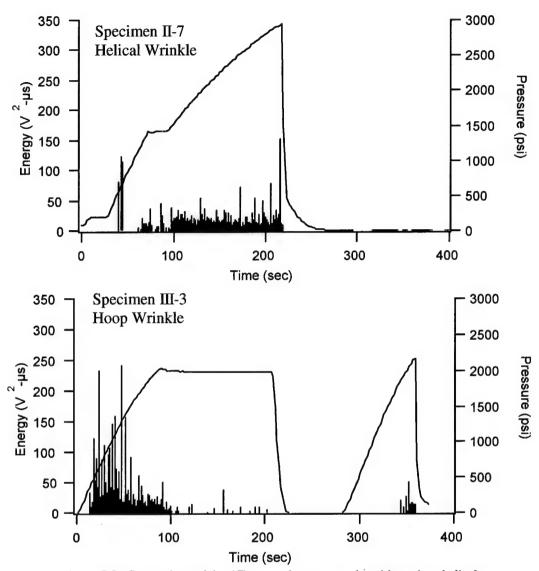


Figure 5.5. Comparison of the AE energy between a tube with a minor helical wrinkle and one with a hoop wrinkle.

hoop-wrinkled tubes with burst strengths below 2500 psi. The hoop-wrinkled tubes had increased acoustic activity in the wrinkle region at pressures well below the helical-wrinkled tubes. However, during the pressurization cycles, none of the tubes in the study generated any evidence of delamination growth even though delamination growth was predicted to occur before burst. At pressurization levels approaching the burst strength of the nominal tubes, a subtle decrease in the acoustic-event generation rate was noted. This signature has the potential to provide an indication of imminent tube failure. However, additional work is required to determine how best to exploit this acoustic data.

The potential for AE as a diagnostic has been proven in a number of production composite programs. The challenge faced in this specific test program and any follow-on testing is to improve confidence

in the predictive capability of AE testing. The experience gained from this test program suggests several approaches for testing to improve the results obtained from AE monitoring. These include the testing of tubes with more severe initial damage. In particular, the damage should tend to grow before the ultimate strength of the tube is reached. Such a flawed tube will provide a better AE development tool. In addition to the redesigned test piece, ultrasonic inspections should be performed following different levels of pressurization. The ultrasonic data will both confirm and correlate the presence of damage in the tube with the measured AE data.

# 6. Modeling and Analysis

### 6.1 Introduction

This section discusses three analysis topics for filament-wound tubes: (1) Behavior of 2-in. and 4-in. tubes using composite laminate theory, (2) Weibull analysis of the strength of the tubes, and (3) Finite-element analysis of stress distributions near hoop wrinkles and helical wrinkles. In conclusion, some general remarks are made about analysis of wrinkles and their effect on composite strength.

## 6.2 Laminate Analysis of the 2-In. and 4-in. Tube Data

The filament-wound tubes in this study were constructed of graphite fibers and epoxy matrix. The resin was Epon 828 epoxy (Shell Chemical), and the fibers were Toho G30-500 carbon filaments in 12K tows. For the first series of tubes (Test Series I, II, and III tubes), the fibers had a modulus  $E_f = 34$  Msi and a nominal tensile strength  $\sigma_f = 550$  ksi. These parameters changed for the last batch of fibers, namely, the Series-IV tubes with large helical wrinkles. For the latter series, the fiber properties were  $E_f = 34$  Msi and  $\sigma_f = 613$  ksi. Typical fiber volume fractions within the tows were  $V_f = 50-60\%$ . The values of  $V_f$  were lower for hoop tows than for axial tows (see Table 6.1).

The filament-wound tubes had two different layups:

- "Mechanical Properties" Tubes: inner diameter = 2 in., 9-ply laminate, layup angles  $[+10, -10, 90]_3$ .
- Series I, II, III Tubes: inner diameter = 4 in., 9-ply laminate, layup angles [+10, -10, 90]<sub>3</sub>.
- Series IV Tubes: inner diameter = 4 in., 12-ply laminate, layup angles  $[+15, -15, 90_2]_3$ .

The angle plies in the tubes, with tows wound at 10° or 15° orientation to the tube axis, are commonly referred to as the "helicals." The 90° plies are referred to as the "hoops." The average ply thickness in all the tubes was 0.008 in. Hence, the 9-ply cylinders had a total wall thickness of 0.072 in., and the 12-ply tubes had a wall thickness of 0.096 in. The Series I, II, III, and IV tubes all had an inner diameter of 4.0 in. However, a small group of "mechanical properties" tubes were also wound with 2.0-in. inner diameter. The purpose of these tubes was to provide some extra property data that was needed for the laminate analysis, e.g., shear modulus G and Poissons ratio v.

Tables 6.1 and 6.2 show the material and ply properties for the 2-in.-dia tubes. This represents the best estimate for the ply properties that causes the predicted behavior to match the test data. The ply

Table 6.1. Fiber and Ply Data for the 2-In. Tubes

### **Fiber and Matrix Properties**

Fiber Modulus: Ef = 34.0 Msi

Fiber Vol. Fractions:

V<sub>f</sub> = 0.56: average value for complete tube

V<sub>f</sub> = 0.60: helical direction

V<sub>f</sub> = 0.50: hoop direction

## Ply and Laminate Data

### Series-I,II,III Tubes (4-in.-dia) and "Mechanical Properties" Tubes (2-in.-dia)

Total No. of Plies: 9

Total Laminate Thickness:

0.072 in.

Lay-up for Series-I,II,III Tubes (4-in.-dia): [+10, -10, 87.9]3 Lay-up for "Properties" Tubes (2-in.-dia): [+10, -10, 85.9]3

Ply Thicknesses (mils) from microscopy:

7.36, 7.48, 8.62, 7.09, 8.11, 8.70, 7.56, 8.74, 8.62 (outer)

#### Series-IV Tubes (4-in diam)

Total No. of Plies: 12

Total Laminate Thickness:

0.096 in.

Lay-up for Series-IV Tubes (4-in diam): [+15, -15, 87.9, -87.9]3

Ply Thicknesses (mils) from microscopy:

(inner) 6.73, 7.24, 8.03, 8.03, 7.44, 7.36, 8.35, 8.35, 7.68, 7.83, 9.55,

9.55 (outer)

Table 6.2. Ply Input Properties for Laminate Analysis

### Single-Lamina Elastic Properties

Modulus, axial direction: E<sub>11</sub> = 20.4 Msi\*

Modulus, transverse direction:  $E_{22} = 0.7 \text{ Msi}$ 

Modulus, cross-ply direction: E<sub>33</sub> = 0.7 Msi

Shear modulus: G<sub>12</sub> = 0.8 Msi

Shear modulus: G<sub>13</sub> = 0.8 Msi

Shear modulus: G<sub>23</sub> = 0.8 Msi

Poisson's ratio:\*\*  $v_{12} = 0.35$ 

Poisson's ratio:  $v_{13} = 0.3$ 

Poisson's ratio:  $v_{23} = 0.3$ 

\*Based on  $V_f$  = 60% for the helical fibers. This value is reduced to  $E_{11}$  = 17.0 Msi for the hoop plies ( $V_f$  = 0.50).

\*\* Nomenclature for Poisson ratios  $v_{ij}$ : "i" dir'n. refers to loading axis and "j" dir'n. refers to transverse (Poisson) strain

thicknesses in Table 6.1 were measured from polished cross sections by optical microscopy; these numbers were input directly in the laminate analysis. In general, the hoop plies were less consolidated than the helicals, hence, the larger ply thickness (and lower volume fraction). Microscopic

analysis confirmed that the hoop fiber volume was indeed lower, by an average of about 9%. However, this figure was based on a very small number of samples. The value of  $V_f = 0.50$  for the hoop plies was obtained by matching the experimental test data with laminate theory.

Table 6.1 lists the exact fiber lay-up angles in each tube. In general, the fiber angles for the helical fibers were found to be quite accurate (either  $10^{\circ}$  or  $15^{\circ}$ ). However, a fiber angle of exactly  $90^{\circ}$  is not possible for the hoop filaments in a filament-wound tube because the winding process creates a spiral geometry. This spiral causes the hoop fibers to be at a slight angle to the circumferential direction. The error  $\alpha$  (angular deviation from  $90^{\circ}$ ) depends on the bandwidth (w) of the tows and the tube diameter (D). Assuming that adjacent tows are just touching, it is easy to verify for a spiral layup on a cylinder that  $\tan[\alpha] = w/\pi D$ . In the present case, the tows of Toho 12K fiber have a width w = 0.45 in. Since D = 2.0 in., this gives  $\tan[\alpha] = (0.45)/(2\pi) = 0.0716$  and so  $\alpha = 4.1^{\circ}$ . The real hoop fiber angle in the 2-in. tube is, therefore,  $(90 - 4.1) = 85.9^{\circ}$ . A similar calculation for the 4-in.-dia tubes gives a real hoop fiber angle of  $87.9^{\circ}$ . These values were used in the classical laminate analyses for the material properties and the ply stresses.

The 2-in. tubes were cut into test coupons and loaded in tension or torsion. Table 6.3 shows the experimental and predicted properties for the tubes. The apparent agreement simply reflects the fact that some of the input properties, especially the transverse E and shear stiffness G, were adjusted so that the theoretical predictions matched the experimental data. A discrepancy does exist for the predicted Poisson's ratio: the experimental value is about 26% higher than the analysis. The two most plausible explanations for this difference are: (1) the cylindrical geometry of the tubes, and (2) extraneous forces acting on the test specimens. The first error is related to the curvature of the tubes since the laminate analysis assumes that the material is a flat plate. The 2-in.-dia tube has a significant curvature, which could cause some deviations in the strains due to the round geometry. The second source of error could occur if extraneous forces were applied to the test specimens during loading; e.g., if the tensile specimens were subjected to extraneous torques from the grips of the test machine. However, there was no evidence from the strain gage data that such unexpected loads were present. Hence, the most plausible explanation for the discrepancy is curvature effects in the specimens.

Table 6.3 Test Data and Predictions for 2-In. Tubes

Property	Measured Experimental Properties	Properties from Laminate Analysis
Tensile Modulus (E)	12.5 <b>M</b> si	12.6 Msi
Shear Modulus (G)	1.1 <b>M</b> si	1.13 Msi
Poisson's Ratio (v)	0.13	0.096

Tables 6.4 and 6.5 show the predicted ply stresses for tubes without wrinkles. For the 9-ply tubes (Series I, II, III), the internal pressure was set to 2860 psi in the analysis. This was the average value for the burst pressure of 9-ply tubes without wrinkles (see Table 6.6). In general, for a thin-wall tube, the wall stresses become:

Hoop direction stress:

 $pR/t = (2860 \times 2)/0.072 = 79,444 \text{ psi}$ 

Axial direction stress:

 $pR/2t = (2860 \times 2)/(2 \times 0.072) = 39,722 \text{ psi}$ 

Table 6.4. Calculated Ply Stresses in Series-I,II,III Tubes (4.0 in Diameter, 9-ply) Loaded to 2860 psi Internal Pressure

Ply Stresses and Strains in Hoop Fiber Direction		
Layer	Stress	Strain
Hoop layer 3	220,393 psi	1.29%
Hoop layer 6	220,626 psi	1.29%
Hoop layer 9	220,870 psi	1.29%
Ply Stresses and Strains in Helical Fiber Direction		
Layer	Stress	Strain
Helical layer 1	31,551 psi	0.138%
Helical layer 2	60,771 psi	0.282%
Helical layer 4	45,208 psi	0.204%
Helical layer 5	74,532 psi	0.349%
Helical layer 7	59,337 psi	0.273%
Helical layer 8	88,984 psi	0.420%

Table 6.5 Calculated Ply Stresses in Series-IV Tube (4.0 in Diameter, 12-ply) Loaded to 7675 psi Internal Pressure

	•	
Stresses and Strains in Hoop Fiber Direction Ply		
Layer	Stress	Strain
Hoop layer 3	293,180 psi	1.71%
Hoop layer 4	292,336 psi	1.70%
Hoop layer 7	293,367 psi	1.71%
Hoop layer 8	294,201 psi	1.70%
Hoop layer 11	295,280 psi	1.71%
Hoop layer 12	294,485 psi	1.70%
Ply Stresses and Strains in Helical Fiber Direction		
Layer	Stress	Strain
Helical layer 1	93,560 psi	0.41%
Helical layer 2	100,820 psi	0.44%
Helical layer 5	164,701 psi	0.78%
Helical layer 6	160,733 psi	0.82%
Helical layer 9	238,699 ps	1.14%

Table 6.6. Burst Strengths of Unwrinkled Tubes.

Burst Strength (psi)	Comments
2787 psi	Initial batch of unwrinkled tubes.
2850 psi	
2861 psi	u
2869 psi	4
2667 psi	Unwrinkled specimen taken from 2 <sup>nd</sup> batch of tubes *.
2894 psi	Unwrinkled specimens taken from 3 <sup>rd</sup> batch of tubes **
3090 psi	•
<ul> <li>2<sup>nd</sup> batch had helical wrinkles</li> </ul>	
** 3 <sup>rd</sup> batch had hoop wrinkles	

These applied loads were input into a computer program that performs classical laminate analysis. The input data (ply thicknesses, material properties) were drawn from Tables 6.1 and 6.2. Table 6.4 shows that for the given lay-up of the 9-ply tubes, the hoop plies carry the highe`st stresses. According to the laminate analysis, failure would occur when the hoop fibers reach an ultimate strain of 1.29% (equivalent hoop stress equals 220 ksi). The failure strain of individual Toho G30-500 filaments can be computed from the manufacturer's data:  $\varepsilon_{\text{ult}} = \sigma_{\text{ult}}/E = 550 \text{ ksi/34 Msi} = 1.62\%$ . Hence, the real failure strain in the tubes is about 80% of the test data for Toho filaments. The reduction in failure strain in the hardware indicates that additional defects are introduced into the fibers during filament winding. Note that the laminate analysis models the tubes as if they are "flat plates." A more refined analysis (see later finite-element calculations) would take into account the curved geometry. At that time, it becomes clear that the hoop plies do not have identical stresses. In fact, the innermost hoop ply actually carries the highest load, and this is believed to be the site where failure initiates.

The composite laminate analysis here has also assumed "zero curvature" in the hoop direction. The layup pattern of the 9-ply tubes, namely [+10, -10, 87.9]3, is not symmetrical about the mid-plane of the laminate. Hence the stiffness matrix, which connects the in-plane stresses and the laminate curvatures, is non-zero. This matrix is often referred to as the B-matrix in textbooks (Ref. 6.1) on the theory of laminated composites. As a result of the B-matrix being non-zero, when the laminate is loaded in tension it also develops a curvature (according to laminated plate theory). This curvature would cause the ply stresses to take on significantly different values than shown in Tables 6.4 or 6.5. However, in this instance, the predicted curvature is not correct. Pressurized composite cylinders do not exhibit a change in curvature around the hoop direction, nor do they develop a curvature distortion term. This is due to the symmetry of the circular cross-section of the cylinder and the fact that the pressure loading is also axisymmetric. The deformed shape is also circular. Hence, the terms in the laminate analysis corresponding to  $\kappa_{\text{hoop-axial}}$  have been deliberately set to zero, which alters the stress predictions for the plies. In this way, the laminate analysis has been adjusted to make it more realistic for filament-wound cylinders.

Similar calculations were performed for the 12-ply tubes (Series-IV tubes). These are shown in Table 6.5. In this case, the unwrinkled specimens failed at an average internal pressure of 7675 psi. Table 6.5 indicates that the strains in the Toho fibers were around 1.70% at this load. This behavior was at first puzzling since the Series IV tubes appeared to be significantly stronger than earlier batches. However, it was revealed that the graphite filaments in the last series of tubes had significantly different material properties. The new failure strain for individual filaments had increased from 1.62% to 1.80%. Hence, the Series IV tubes were effectively made from a "stronger" material. The "knockdown factor" in the fiber failure strains is 1.70%/1.80% = 0.94. Note from Table 6.5 that the hoop plies still dominate the failure behavior of the tube design. The ratio of the maximum hoop strain to the maximum helical strain is 1.70%/1.19% = 1.43. This is much lower than the hoop/helical ratio for the Series-I,II,III tubes, where the value was 1.29%/0.402% = 3.21. Hence, for all the tubes, it would be expected that a "hoop-dominated" failure mode should occur.

### 6.3 Weibull Analysis of the Strength Data for Unwrinkled Tubes

Figure 6.1 shows the burst data for nine unwrinkled tubes from Test Series I, II, and III. All these tubes had a diameter of 4 in. and were fabricated without any intentional defects (fiber wrinkles). Three of the tubes were directly pressurized to burst. These tubes are referred to as "virgin tubes" and

they are depicted with dark-blue diamonds in the figure. A second group of five tubes was initially proof tested and then burst. The latter tubes are referred to as "proofed tubes" in the plot, and the data are depicted as red triangles. One extra data point in Figure 6.1 is marked with the legend "5-sec stress-rupture burst." This point corresponds to Tube I-9, which failed at constant load (unintentionally) during a proof test. Since this was an initial loading failure, it has been lumped in with the results for virgin tubes. The 5-s rupture was a time-delayed failure, and it appears to be similar to reported cases of stress-rupture failure in graphite-epoxy pressure vessels. Since Tube I-9 was loaded to a very high percentage of the fiber strength, it is plausible that a short-term stress rupture of the fibers could have taken place.

The most interesting feature of Figure 6.1 is the scatter in the data. The virgin tubes had very consistent burst strengths. Three of the data points (blue diamonds) fall almost on top of one another, while the "5-second burst" point is only slightly lower in pressure. However the "proofed tubes" (red triangles) had a much larger variation in their ultimate strength. There are two possible interpretations for this behavior. The first hypothesis states that the two sets of data are drawn from the same population. In other words, the initial proof test is irrelevant, and there was no effect of proof load on the final burst strength of the tubes. The strongest argument in support of this hypothesis is that the averages for the burst strength in each group are very close together (2860 psi for the three virgin tubes vs. 2836 psi for the five proofed tubes). This lends credibility to the idea that all the strength data are simply drawn from the same population, and so proof testing has no real effect on strength.

However, there is another interpretation for the data in Figure 6.1. This second hypothesis states that the difference between the two groups of data is real, as indicated by the wide dispersion in the data scatter. According to this second hypothesis, the two groups are not drawn from the same population, and the proof test does affect the tube behavior. At first sight, the idea is puzzling because of the trend lines (green dotted lines) shown in Figure 6.1. If the trend is real, then some of the tubes would have to become stronger after the proof test (while others become weaker). A possible explanation for this behavior lies in the geometric shape of the tubes. When the tubes are fabricated, they are wound and cured on a circular mandrel. They are then cooled and removed from the mandrel. Ideally, they should remain circular, but it is well known that composite materials can warp or change shape after thermal processing. Such warpage is usually caused by non-uniform internal stresses resulting from curing and thermal contraction. As a result, some of the tubes may not be perfectly round after they are removed from the mandrel. The "circularization" hypothesis argues that the

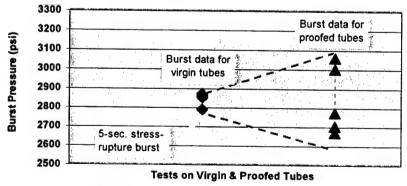


Figure 6.1. Burst data for tubes w/o wrinkles.

proof test actually improves the shape of these tubes and restores it to a more perfect circle. The symmetrical loading of an internal pressurization test may tend to "circularize" the fiber geometry, leading to higher burst strengths. If this is true, then a proof test will cause a wider scatter in the burst strengths. Some tubes will be stronger (due to circularization) while others may be weaker (material damage caused by the high proof loading).

There is some evidence to support the idea of "circularization" during proof. First, within the rocket industry it is known that filament-wound motor cases change their cross-sectional shape after proof loading. Manufacturing engineers have discovered that if composite segments are proof loaded, then they tend to become more circular, i.e., closer to a perfect circle. Anecdotal evidence for this is that bolt holes are more likely to match up between neighboring segments after proof testing. A second piece of evidence to support "circularization" comes from the experimental deformation studies in this report. Moiré fringe measurements have shown that some of the tubes tend to "pop-in" during pressurization, meaning that the tube wall adopts a more circular geometry, and shape defects are removed. The change is permanent after unloading and presumably leads to increased burst strength. Other tubes do not undergo such a "pop-in" correction, and these tubes were discovered to have larger strain irregularities in their walls during loading. Currently, it is not known exactly why some tubes exhibit this phenomenon while others do not.

The circularization hypothesis is interesting and may explain the trend lines shown Figure 6.1. However, it is clear that the average burst strength is unaffected by proof testing, regardless of which hypothesis is valid. Hence, it is reasonable to conclude that proof testing has no noticable effect on burst strength. Based on the "worst-case" envelope in Figure 6.1 (lower green line), we could expect a maximum strength reduction of 7–8% for some of the tubes that were proof tested.

The burst data for seven unwrinkled tubes are in shown in Table 6.6. This table extends the data in Figure 6.1 (blue diamonds) by adding an extra five burst tests. The extra tests were also on virgin tubes without wrinkles. Figure 6.2. shows the data in statistical form, where the x-axis represents internal pressure, and the y-axis plots the cumulative probability of failure. The Weibull curve that fits the data (dotted orange line) is associated with the following parameters: Weibull slope m = 23.8, and scale parameter  $\sigma_0 = 2953$  psi. The fit is not unique, and it is possible to argue that "m" may

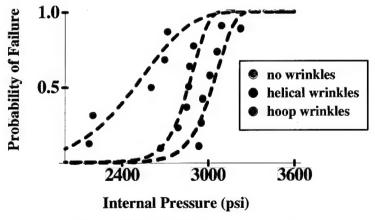


Figure 6.2. Weibull Plots for burst strengths of tubes.

range as high as 30 and that  $\sigma_0$  may drop down as low as 2920 psi. However, it does appear from the plot that the complete set of data in Table 6.4 is drawn from one overall family.

Figure 6.2 also shows Weibull plots for the strength of tubes with hoop wrinkles (green curve) and tubes with moderate helical wrinkles (blue curve). Two features of the data become clear from the Weibull plots. First, the tubes without wrinkles show a similar behavior to the tubes with minor helical wrinkles, except that the helical wrinkle data are shifted to the right. In other words, strength values for the blue curve are increased by a constant value. It is unlikely that minor wrinkles in the helical fibers actually strengthened the tubes. It is much more likely that this batch of specimens (minor helical wrinkles) was made with fibers that had a slightly higher failure strain. Hence, the blue and orange curves would overlap one another and become one family if corrections were made for fiber strength differences between the specimens.

Second, it is clear that the hoop wrinkles (green line in Figure 6.2) cause a behavior that is quite different from the other specimens. There is a significant strength reduction for the green line, which is manifested as a shift to the left on the plot. There is also a much wider dispersion of the strength data, shown by a lower slope of the Weibull line at the 50% level. It follows that hoop wrinkles cause a failure mechanism that is quite different from standard bursts of tubes with no wrinkles, or minor helical wrinkles.

# 6.4 Finite-Element Analysis of Tubes with Wrinkles

### 6.4.1 Introduction

The finite-element analyses in this study looked at hoop wrinkles and helical wrinkles in filament-wound tubes. The scope of the study was limited to linear elastic analysis. In some instances large-deformation theory was applied, but there was no incorporation of nonlinear material behavior. The predictions from linear stress analysis are compared with experimental data for tube burst pressures and strain gage responses. In the case of helical wrinkles in tubes, the agreement between the predicted and measured burst strengths is quite good. In other cases, the finite-element analysis underpredicted the burst strength of the wrinkled tubes. This is to be expected since linear elastic models tend to exaggerate the effects of stress concentrations within materials. Often these stress risers are blunted by processes such as "yielding" behavior or the growth of multiple crack fronts. Predictions in this section could be improved in the future by including models for progressive crack growth in composites.

## 6.4.2 Wrinkle Modeling

The finite-element method (FEM) was used to perform two detailed analyses of wrinkles in tubes. In the first case, an FEM model was constructed for a large helical wrinkle in a 12-ply tube (Figure 6.3). The figure shows a cross-section in the axial-radial plane, with the axial direction being horizontal and the radial direction being vertical. In Figure 6.3, the blue regions represent the helical plies, the red regions represent the hoop plies (with some hoops being displaced near the wrinkle), and the yellow regions represent the matrix material. The horizontal axis in the figure corresponds to axial distance along the length of the tube, and the vertical axis corresponds to radial thickness across the wall. The third direction, into the paper, would be the hoop fiber direction. A distortion resembling a sine

wave was placed in the middle helical ply. The wave shape was not perfectly symmetrical; the exact coordinates were taken from photographs of the cross-sections of Series-IV tubes. The effect of the wavy helical fibers is to reduce the effective axial stiffness of the tube in the neighborhood of the wrinkle. Note that the hoop fibers were assumed to remain circular in this model (i.e., circular around the circumference of the tube). However, it was necessary to shift some hoop fibers laterally, either left or right in Figure 6.3, so as to accommodate the helical wrinkle. This localized shifting of hoop fibers is referred to as "hoop thinning" because it leads to apparent weak spots in the hoop fiber reinforcement. The process is not simply a modeling artifact because hoop thinning is actually observed in filament-wound composite tubes with large wrinkles (see Figure 4.12). In Figure 6.3, it can be seen that there are no fibers in the second hoop ply (red) near the apex of the wrinkle. One of the goals of this analysis was to see whether "hoop thinning" actually causes a decrease in burst pressure for the tube. Note that in Figure 6.3 the helical wrinkles are assumed to run fully around the circumference of the tube; i.e., the wrinkle is axisymmetric in geometry. Figure 6.3 shows only a part of the full mesh used to simulate the tube and wrinkle (the central portion). The real models extend both on the left and the right. The nodes at the left end of the model were fixed axially, and an axial tensile stress was applied at the right end. This modeling condition simulated the axial load in the tube wall caused by internal pressurization.

It is important to mention ply thinning effects in Figure 6.3 and the way in which fiber volume is conserved. Clearly, when hoop thinning occurs there can be no fibers lost in the model. Hoop fibers may be shifted laterally, or piled up locally into higher concentrations, but they cannot leave the model completely. Therefore, the fiber volume fraction must be altered to account for changes in the thickness of the hoop plies. In the present case, this was done using an "integrated approach;" i.e., the hoop fiber volume fraction was scaled so that when it is multiplied by the true area of the hoop plies, the correct number of hoop fibers is obtained. Consequently, the total volume of hoop fibers in the cross-section is just the same as if no wrinkle was present (defect-free tube).

The second FEM model looked at a large hoop wrinkle in a 9-ply tube (Figure 6.4). This model included two graphite-epoxy rods within the resin pockets of the composite. These were real rods that were placed into tubes in Series III to cause wavy distortions in the hoop fibers (see Figure 4.8). The model assumes that only the hoop fibers are wavy; the helical fibers remain straight. A generalized plane-strain analysis was used for this configuration, with the wrinkle placed at the middle of a 180° arc. The nodes at the ends of the arc were constrained from moving circumferentially, but were free to move radially under the influence of internal pressure. These boundary conditions are an approximation to the stress solution for the real cylinder. By applying symmetry conditions on the

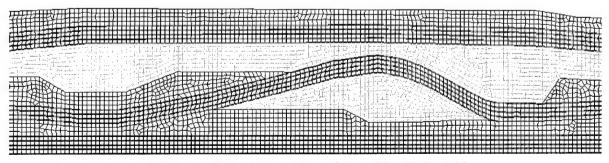


Figure 6.3. Finite-element model of tube with helical wrinkle.

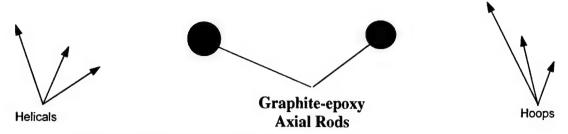


Figure 6.4. Finite-element model of 9-ply composite tube with hoop wrinkles.

boundary, the cylinder is actually modeled as if it contains two 180° segments, each of which contains a wrinkle defect. However, because the length of the defect is small (roughly 10° to 15°), it is believed that the symmetry boundary conditions do not cause a large error in modeling. Hence, the present approach was used to allow high mesh refinement for the finite-element model in the vicinity of the hoop wrinkle. The imposed strain in the third direction (axial direction of tube) was such that the axial stresses were consistent with loads in a pressurized thin-walled cylinder. The large-displacement option was used during the FEM analysis because the strain results were noticeably sensitive to element deformations. Physically, this corresponds to the situation where the innermost hoop wrinkle straightens out under pressure. The large-displacement analysis allows the model to reproduce this effect.

The ABAQUS commercial finite-element code was used in both FEM models, with linear elastic material behavior. Four-node quadrilateral elements (linear quads) were employed throughout the mesh, except at a few localized areas, which necessitated triangular elements. Since 2-D models were used, it was not possible to represent the complete 3-D layup of the tubes. Hence, the fiber angles of the helicals could not be input into the models. Instead, the helical plies were replaced by equivalent axial plies with the same axial stiffness as either a  $[+10^{\circ}, -10^{\circ}]_{s}$  or a  $[+15^{\circ}, -15^{\circ}]_{s}$  angle-ply laminate.

# 6.4.3 Analysis Results for Helical Wrinkle in 12-Ply Tube

The predicted strains in the hoop fibers are shown in Figure 6.5 for an internal pressure of 7675 psi. This value was a preliminary estimate for the average burst pressure for tubes from Series IV (tubes without wrinkles). After all testing was completed, the actual average burst presure was 7653 psi. However, the difference between the two values is very small (0.3%), so for all practical purposes, the analysis results below are representative of a typical composite tube. The figure shows strain as a function of axial station along the cylinder. The zero position is midway between the two rods.

Also shown in Figure 6.5 is the helical wrinkle geometry (exaggerated scale for clarity). The purple section of the wrinkle is the region of hoop thinning. Through-thickness variations in strain for each winding are shown on the plot. As expected, the largest hoop strain occurs at the ID of the innermost hoop ply. The maximum predicted strain away from the wrinkle area is 1.65%. This value is fairly close to the earlier prediction from composite laminate analysis (Table 6.5) (maximum strain in hoop fibers = 1.70%).

At the location of the wrinkle, the FEM model predicts a maximum hoop strain of 1.74% at the innermost hoop ply underneath the right-hand side of the wrinkle. Hence, the strain concentration

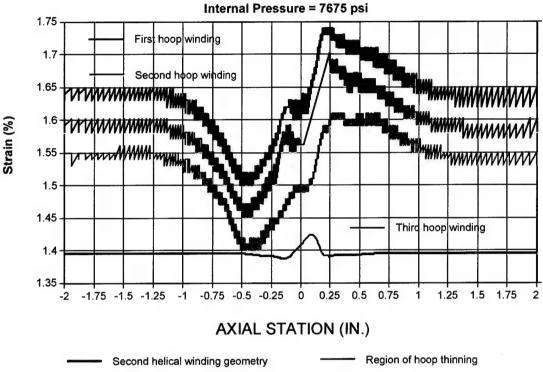


Figure 6.5. Predicted hoop strains in 12-ply tube with a helical wrinkle (Series IV).

factor caused by the wrinkle is:  $S_{\epsilon} = 1.74\%/1.65\% = 1.054$ . It follows that tubes with helical wrinkles should fail at a burst pressure given by:  $p = 7675 \text{ psi/S}_{\epsilon} = 7675 \text{ psi/}(1.054) = 7282 \text{ psi}$ . This predicted burst pressure value is only slightly higher (3%) than the average burst pressure of 7078 psi for the three tubes from Series IV that contained helical wrinkles. Thus, the FEM analysis predicts the burst pressure of tubes with helical wrinkles fairly well.

Figure 6.6 shows the predicted strains in the helical windings. The average helical strain away from the wrinkle is about 0.87%. This agrees with the laminate analysis in Table 6.5 fairly well if the strain at the midsection of the laminate (0.82%) is taken. It is clear that the laminate analysis overpredicts the variation in helical strains across the tube wall. This reflects the fact that the laminate analysis represents the tube as a flat plate, and bending effects are much larger for cylindrical specimens. In Figure 6.6, the second helical ply contains the wrinkle. As expected, there are large variations in strain near the wrinkle region, especially at the right-hand side of the wrinkle where the curvature is sharpest and hoop thinning is present. The strains are not, however, near the ultimate strain capability of the fibers.

The interlaminar shear stresses in the helical plies are shown in Figure 6.7. The stresses are fairly benign, except in the region of high curvature near the wrinkle. The large shear stresses could, in principle, induce a delamination. One of the puzzling aspects about the present investigation is why delamination cracks did not grow at the wrinkle under high loads. No significant AE emissions were recorded that could be associated with large-scale delamination growth. Other aspects of the tube failures, such as the high burst pressures, are also consistent with the absence of large-scale delamination.

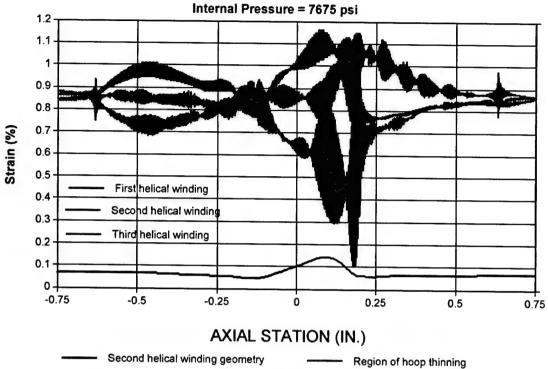


Figure 6.6. Predicted helical strains in 12-ply tube with a helical wrinkle.

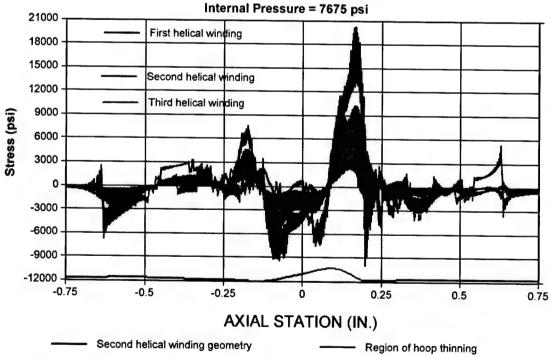


Figure 6.7. Predicted interlaminar shear stresses in 12-ply tube with a helical wrinkle.

nation cracks. Apparently some other factor must have reduced the tendency for delamination, in spite of the high shear peaks in Figure 6.7. It is possible that the cross-ply stress, which is under compression, may play a role in reducing delamination.

Strain gages were employed on two tubes from Series-IV: specimen IV-1, which had no wrinkles and which burst at 7630 psi; and specimen IV-2, which contained a helical wrinkle and burst at 7177 psi. A single rosette gage was employed on the outer hoop ply of specimen IV-1. This gage measured hoop, axial, and 45° off-axis strains. Two such gages were employed on specimen IV-2, one near the wrinkle and one far away from it. The predicted hoop strains on the surface of a specimen with a helical wrinkle are shown in Figure 6.8, along with the strain gage data (normalized to a pressure of 7675 psi). The FEM analysis gave a hoop strain of 1.53% on the outer surface of the tube, away from the wrinkle. The measured strain for an unwrinkled specimen is 1.49%. Hence, the far-field strain predictions are in good agreement with the data, with an error of only 3%. At the wrinkle location, the hoop strain was calculated to be in the range 1.4–1.6%. This compares with an experimental value of 1.39% (adjusted to a pressure of 7675 psi). Since the strain gage has a length of 0.0625 in., it averages strains over a short dimension. Therefore, the experimental data cannot capture the highest peaks in the strain field. Considering these factors, the agreement between predictions and experiments at the wrinkle looks good.

The corresponding results for the axial strain gages are shown in Figure 6.9. The measured axial strain for the unwrinkled tubes at burst (specimen IV-1) was actually 0.92%. However, during the ramp in pressure there was an abrupt change in strain of +0.1%. This may have been due to local resin cracking beneath the gage since the outer hoop ply is weak in the axial direction. When this abrupt change in strain is subtracted from the measured strain at burst, then scaled to 7675 psi, the resulting strain is 0.82%. This value is within 3% of the predicted strain of 0.80%. Thus, there is again excellent agreement between the test and analysis results for an unwrinkled specimen.

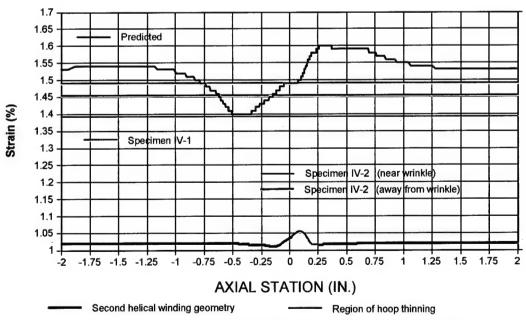


Figure 6.8. Outer surface hoop strains in 12-ply tube with a helical wrinkle, scaled to 7675 psi internal pressure.

The measured axial strain (scaled to 7675 psi) away from the wrinkle (specimen IV-2) is 0.97%, which is 18% larger than the corresponding scaled measured strain of 0.82% for the unwrinkled specimen. Hence, there is some inherent variability in the strain gage data, which might reflect uneven bonding of the gages to the tube surfaces or instrumentation errors.

The predicted axial strain at the wrinkle varies greatly, especially near the crest of the wrinkle, as shown in Figure 6.9. The scaled measured strain (specimen IV-2) for the gauge near the wrinkle is within this range, though on the high side. No firm conclusions can be drawn on the accuracy of the analysis for axial strains at the wrinkle, given the variability in the experimental data.

# 6.4.4 Helical Wrinkle Analysis Parametric Studies and Results

Parametric studies were performed to determine the sensitivity of the helical wrinkle analysis to the following issues: (i) modulus of the matrix in the resin pockets, and (ii) local variations in the stiffness of the hoop plies (caused by fiber bunching). The results of the study showed that resin pocket modulus had little effect on the predicted stresses, but changes in the hoop stiffness did significantly affect predicted burst pressures. Thus, for correct modeling of hoop thinning, the hoop stiffness must be locally adjusted to account for fiber bunching.

A third study looked at burst predictions when "hoop thinning" was not present; i.e., the wrinkle geometry was kept the same, as in Figure 6.3, but the hoop plies were all left intact. Surprisingly, the analysis results still showed an increase in the peak hoop strain in the vicinity of the wrinkle. The peak strain was 1.71%, and occurred about 0.75 in. away from the apex of the wrinkle. This value is close to the 1.74% predicted when hoop thinning was present. It follows that the strain amplification

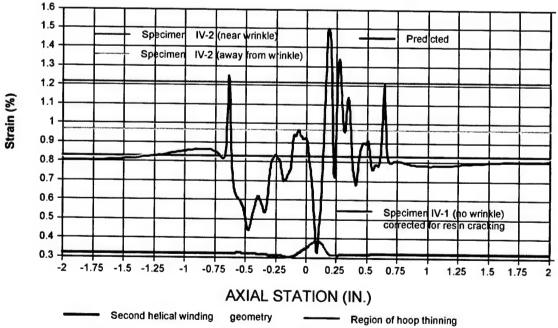


Figure 6.9. Outer surface axial strains in 12-ply tube with a helical wrinkle, scaled to 7675 psi internal pressure.

at a wrinkle must be caused primarily by bending and stiffness distortions associated with the wrinkle geometry. The secondary effect of "hoop thinning" does not contribute significantly to a reduction in burst pressure. It is important to note, however, that this conclusion could be different if the hoop thinning existed over a greater length scale (axial direction) in the tube. Evidently, the composite is able to re-distribute stresses caused by hoop thinning, provided these are localized in extent.

Finally, a single-step, progressive damage analysis was performed to see whether a failure mode that was initiated by hoop fiber failure would switch to become a helical failure mode. This study was performed because one of the tubes from Series-IV appeared to exhibit a "mixed-mode" failure, where the initial crack was inclined at some angle to the axial direction of the tube. However, the analysis results show that failure will progress to the next hoop winding, instead of transferring to the helical windings. Unfortunately, it is not clear from the experimental data whether progressive failure occurred in the hoop windings or the helical windings. The camera that records failure can only view the outside surface of the tube, so the early sequence of crack growth is invisible. Finite-element analysis clearly establishes that failure should begin at the innermost hoop ply.

# 6.4.5 Analysis Results for Hoop Wrinkle in 9-Ply Tube

Figure 6.4 shows the geometry for the hoop wrinkle model, and Figure 6.10 presents the strains in the hoop fibers for an internal pressure of 2716 psi (burst pressure of Tube III-6, which was proof tested six times to 2125 psi prior to final burst). The largest hoop strain occurs on the innermost hoop winding. This follows the same trend as the analysis for helical wrinkles. The maximum predicted far-field strain (away from wrinkle) was 1.11%. The maximum predicted hoop strain at the wrinkle location was 2.35%, which occurred in the left-hand resin pocket (where the curvature of the inner hoop winding is sharpest). Thus, a bending failure is expected in this region due to the curvature of the hoop fibers around the resin pocket. The predicted burst pressure of a tube with a hoop wrinkle,

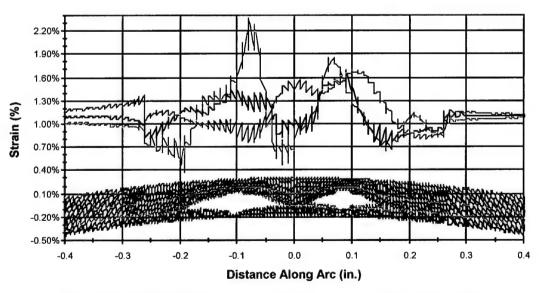


Figure 6.10. Predicted hoop fiber strains for hoop wrinkled tube ran at 2716 psi.

based on data for tubes without wrinkles, is (1.11/2.35) x 2716, or 1283 psi. This value is much lower than the burst pressures of four specimens containing hoop wrinkles: 2195 psi, 2168 psi, 2695 psi, and 2716 psi. Hence, there is a wide discrepancy between the analysis and experiments for tubes with hoop wrinkles.

Looking at the data on burst strengths for tubes with hoop wrinkles, it is seen that there is a wide scatter in the numbers. Furthermore, the data appear to fall into two groups: 2168 psi, 2195 psi; 2695 psi, 2716 psi. This suggests that either the tubes did not fail from identical damage mechanisms, or that the wrinkles within the tubes were not consistent in size (perhaps two different placings of the spacing rods that create the wrinkles). For a tube with a wider wrinkle zone, the curvature of the innermost hoop winding is less sharp. This would lead to lower hoop fiber strains in the innermost layer, and a potentially higher burst pressure. The actual spacing of the axial rods in each specimen was not determined before testing, and there were no sizable remnants of the tubes after burst.

The predicted interlaminar shear stress results are shown in Figure 6.11. The stresses vary greatly over the entire wrinkle region, reversing in sign several times. The regions of peak shear stresses are very narrow, and it seems plausible that small local delaminations could have formed within the tube wall. Just as for the case of helical wrinkles, there was no experimental evidence that any significant delamination cracks grew during testing. Hence, the analysis reaches the same puzzling conclusion as for helical wrinkles. Based upon the shear stress peaks, it seems as if delamination and progressive damage should have occurred in the composites, prior to final burst of the tubes. This is clear from Figure 6.11 because the peak shear stress is 24 ksi, which exceeds typical interlaminar strengths in these composites. Hence, the progressive damage mechanism was inhibited, for reasons that are unknown.

The deformation plot in Figure 6.12 indicates that internal pressurization of the tube causes the innermost wavy hoop ply to straighten out. The middle hoop winding, which is also initially wavy, deforms in a similar manner. It follows that the outer surface of the tube bulges radially when the tube is pressurized. Experimental evidence, particularly Moiré fringe measurements, has confirmed

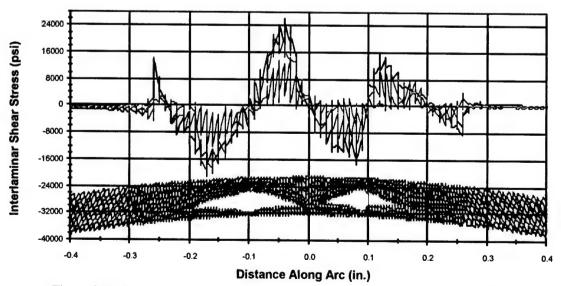


Figure 6.11. Predicted interlaminar snear stresses for noop wrinkled tube ran at 2716 psi.

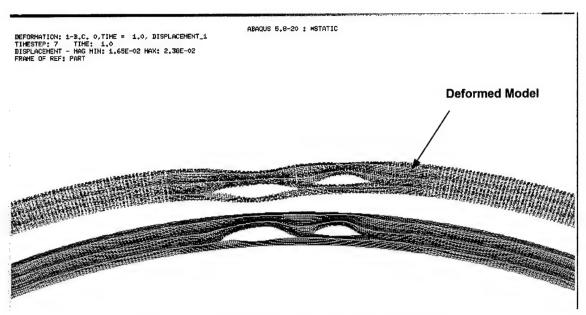


Figure 6.12. Displacement results with 15% magnification.

the existence out-of-plane displacements in the tube surface during pressure tests. This result is significant because it indicates that internal wrinkles in composite cylinders might be detected during proof tests if some type of whole-field strain analysis is done on the specimen surface. The technique is likely to be most effective for wrinkles that are not buried too deep in the cylinder wall. The present analysis model shows significant bulging because the tube wall is thin, so bending deformations are more likely.

A limited comparison is possible between the predictions and the experimental strain data. Two tests were conducted on tube specimens with strain gages. Specimen II-2 was a 9-ply configuration with a shallow helical wrinkle. Shallow helical wrinkles were found to have no significant influence on tube burst strength. So the data from this tube can be used for far-field strain comparisons. As indicated in Figure 6.13, the hoop fiber strain in specimen II-2 (pressure of 2716 psi) is 1.009%. This is only 6% lower than the predicted strain of 1.075%. Specimen III-6 contained a hoop wrinkle, and burst at a pressure of 2716 psi (after six proof test cycles to 2125 psi). The corresponding strain measurement was 1.099%, which is only 2% above the predicted strain. Thus, there is excellent agreement between the test results and the analysis predictions for far-field strains. The 8% difference between the strain gage readings for specimens II-2 and III-6 is likely due to material variability since the specimens were cut from different tubes.

The measured strain at the wrinkle for specimen III-6 (at burst) was 1.172%. The corresponding predicted strains vary from 1.16 to 1.53% over the region of the wrinkle. Thus, the measured strain is within the predicted range, near the lower end. As was noted earlier, it would be expected that the strain gauge averages out localized strains due to the length of the gage. Hence, the comparison between experimental and analysis results is not unreasonable.

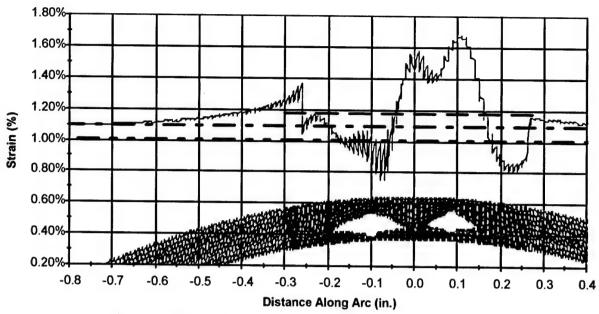


Figure 6.13. Outer surface hoop strains in 9-ply tube with hoop wrinkles.

It is believed that the main reason why the analysis does not do a better job of predicting the burst strength of tubes with hoop wrinkles is due to localized damage in the composite. High strains within the hoop fibers are associated with localized bending, where the wavy plies have a high curvature. These high strains might be reduced considerably if small delaminations stopped the transfer of bending strains into the plies. However, modeling this effect would call for a detailed progressive damage package, which was beyond the scope of the current study. Therefore, future attempts at refining the predictions for burst pressures will need to include nonlinear effects and progressive crack formation within composites. It is also possible that the placement of the axial rods caused some discrepancies between theory and experiment. The analysis used an average position for the rods, but there was some variation on a specimen-to-specimen basis.

# 6.4.6 Hoop Wrinkle Analysis Parametric Studies and Results

Two parametric studies were conducted to determine the sensitivity of the analysis results to these parameters. In one study, the hoop stiffness was not corrected for bunching of the hoop windings in the wrinkle region surrounding the resin pockets. The error in the hoop strain predictions increased, after the correction was removed from the analysis. In another study, the transverse Young's modulus of the graphite-epoxy rods was replaced with the modulus for epoxy resin material. The predicted results for stresses showed little sensitivity to the change in material properties.

# 6.5 Conclusions of Modeling Efforts for Wrinkles

 A hypothesis has been proposed that proof testing of filament-wound tubes may actually strengthen some of the tubes by circularizing their shape. The conjecture is interesting, but needs confirmation in the future on larger batches of specimens.

- Finite-element analyses of the tubes with wrinkles had mixed success in predicting experimental results. The analysis of the tubes with helical wrinkles produced quite good agreement with experiments (experimental reduction in burst strength was 8%, while the predicted drop was 12%). However, the analysis of the tubes with hoop wrinkles overestimated the strength reduction significantly. The most likely explanation is that elastic analysis (including large deformation theory) is inadequate for predicting burst strength. Inelastic phenomena, such as growth of delamination cracks at the microscale level, tend to blunt the stress concentrations within the composite.
- The analytical results indicated that the tubes should develop large delaminations prior to ultimate burst. However, this did not appear to occur experimentally. Therefore, more research is needed for the delamination criteria in filament-wound vessels containing defects.
- Time-delayed failure was observed for one specimen during the tests. It does not appear
  that the wrinkles in the tubes in this study were a significant source for a time-dependent
  failure behavior. However, there is reason to believe from other studies of large-scale
  filament-wound cylinders that defects in the ply structure can cause time-delayed failure.

# 7. Optical Diagnostic Methodologies

Two diagnostic techniques, shadow Moiré and speckle interferometry, were adapted to observe surface deformations of the graphite-epoxy tubes undergoing deformations during pressurization tests. Defect-free and hoop-wrinkle specimens were studied.

#### 7.1 Shadow Moire

Shadow Moiré uses the self-alignment of shadows cast by a fine-pitch grating onto the tube surface with the grating itself to produce Moiré fringes. Moiré fringes are caused by the relative amounts of alignment of the shadow of the grating and the grating itself. The fringe is dark when the shadow of the grating and the transparent portion of the grating line up. When the dark portion of the grating and its shadow line up the fringe is light. Thus, the Moiré fringes are defined by a series of alternating aligned or mis-aligned shadow-to-grating alignments. The Moiré grating or height contour interval is given by,

Height interval = 
$$P \cot(\theta)$$
,

where P is the pitch or period of the grating used and the observation angle  $\theta$  is the angle shown in Figure 7.1. A grating with pitch P = 0.010 in. and observation angle of 65° was used.

In the configuration used, it is capable of forming height contours with a 0.114-mm (0.0045 in.) difference. To enable the monitoring of a large surface area, the grating was curved into a cylinder to closely match the cylindrical surface contour of the tube. This has the effect of removing the height difference of a

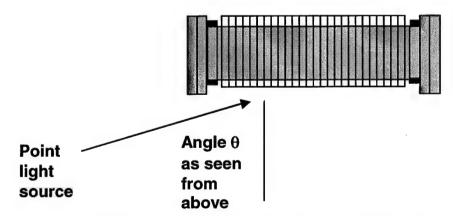


Figure 7.1. A cylindrically curved grating with grating lines perpendicular to the cylinder axis is placed in close contact with the surface of the cylindrical tube. The angle  $\theta$  is the normal incidence angle in the plane defined by the light source, tube axis, and camera observation location.

flat grating to a cylindrical surface, in effect, unwrapping the global curvature of the tube to first order. A zone 1.5 in. wide perpendicular to the tube axis can be monitored in this geometry.

For large pressure changes on the order of 2000 psi, the expected radial change in height of the graphite tube used in this study is 0.5 mm. However, for the purposes of defect detection, a local deformation is expected. The local defect, which would weaken the wall, is expected to deform in height by a quantity inversely proportional to its strength. The 0.5-mm height difference from pressurizing the tube is expected to cause a 4-fringe change. Assuming that we can detect a 0.5 to 1 fringe change, this corresponds to a change in strength of 12–25%. However, if detection of the local defect takes place at a lower value, say 1000 psi, then the sensitivity is proportionally reduced to 25–50%. These sensitivities are sufficient to establish the shape at pressure levels of 2000 psi or greater.

# 7.2 Speckle Interferometry

Speckle interferometry uses the interference pattern of two laser beams, one of which interrogates the surface being sensed while the other acts as a reference. In our version, the interference pattern is captured as an electronic image and is subtracted from a second image in which the tube's surface is subjected to a small change in pressure causing deflection (Figure 7.2). The result is an inteferogram caused by the deflections in the plane of the image. The sensitivity is large, with fringe intervals of  $\lambda$ 2, where  $\lambda$  is the wavelength of light used, 632 nm. The fringes form contours of transverse translation of the second image from the first image. It does not measure height changes directly, but height can be inferred by performing measurements orthogonal to the observation direction. For a perfect cylinder undergoing a uniform expansion, the fringe spacing will be proportional to the product of the radial dimension change and the sine of the angle measured to the position of the surface from the observation direction. Similar to the shadow Moiré diagnostic, the critical information derived from the speckle images is the shape and magnitude of the deformation, which identifies the nature of the defect.

Once the methodologies used for these techniques are verified, a novel diagnostic for predicting failure strength of motor cases may be developed. In addition, the locations of any defects may also be identified.

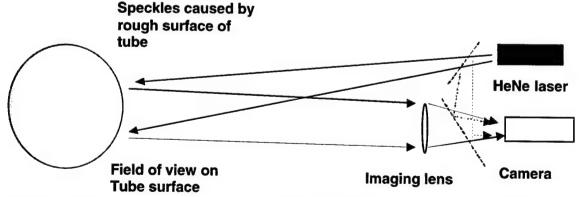


Figure 7.2. Schematic for speckle interferometry. The interference of the reference beam with the image of the scatter beam from the test object is recorded by the camera. Two images, one with no deformation and the other with deformation, are subtracted to give the interference fringes.

## 7.3 Sample Preparation

Tube samples using swaged end fittings and details of the defects are described in Section 3.1. The tubes were sprayed with aluminum paint to preserve the polarization of the scattered light for the speckle interferometry. The outer surfaces for tubes undergoing shadow Moiré were sanded to remove sharp discontinuities. By feathering or tapering the edges, the Moiré fringes can be traced in a continuous manner across the height discontinuity.

### 7.4 Results

### 7.4.1 Shadow Moiré Results

Moiré fringe data were taken of tube III-5 with a hoop wrinkle defect undergoing pressurization up to its ultimate burst strength. The zero pressure images showed the presence of the outside surface deformation induced by the two inserted rods causing the hoop wrinkle. The extent of the zone is consistent with the cross section of the wrinkled zone. The lay-up of the hoop fiber wraps is asymmetric. Of the 3 hoop layers, 2 pass over one rod and 3 pass over the other rod. (See Figure 7.3.) Thus, radial deformation is expected to be non-uniform. It is predicted that once the wall of the tube experiences a bending stress due to pressurization, the rod with only two layers over it will begin to be forced outward since the third layer is under it. The tubing walls are not uniform in thickness; hence, only a small pressure change is needed to cause a local bend.

When the tube is unpressurized [Figure 7.4(A)], a plateau is observed defined by the two rods. As pressure was increased, the height contours showed that more deformation was occurring in the vicinity of a single rod in an asymmetric sense in agreement with prediction of deformation. In the vicinity of the non-protruding rod, the plateau is observed to disappear and is virtually indistinguish-

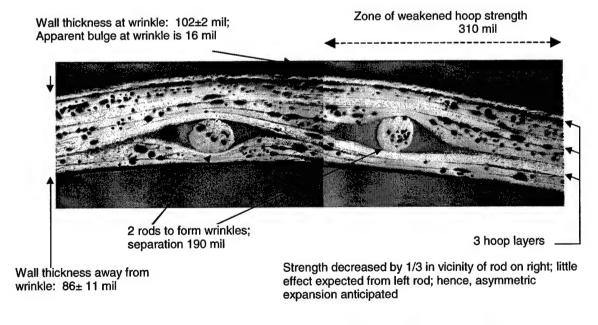


Figure 7.3. Cross section of 4-in. tube with hoop wrinkle. There are 3 hoop layers of which a single layer, the innermost, is under the right hand rod.

able from the rest of the tube [Figure 7.4(C)]. When pressure exceeded 1500 psi, the deformation collapsed such that only deformation around one rod remained. This ridgeline continued to be observed for other intermediate pressures through the last image obtained at 2500 psi. The tube ultimately failed at 2695 psi at the rod wrinkle indicated by the ridge of deformation at the rod. Thus, at 50% of the average burst pressure of a defect-free tube, the spatial location of the deformed zone conformed to that observed at 83% of the average burst pressure. The tube broke at 90% pressure. No acoustic measurements were performed.

Tests were also performed on the backside, 180° away from the location of the defects prior to rupture of the tube at lower pressures. The tube contours were very uniform.

During the pressure tests, other types of localized deformations were observed. Transitions for these deformations occurred rapidly. Visual observations showed the tube undergoing a "pop" to the new contour. Unfortunately, no time recordings were performed since the phenomenon was unexpected. They occurred about every 100–200 psi from 0–1000 psi then slowed down, occurring every 500 psi above that. It should be emphasized that once the tube is pressurized to a given level, this behavior can only be observed when the tube is pressurized above that level. Hence, this phenomena is a new tube behavior.

As Moiré measures contour interval differences only, the sign difference of the intervals is indeterminate. Hence, whether the surface is going up or down is indeterminate. Thus, the asymmetrical deformations observed are consistent with deformation contour in which at 2500 psi, a single high ridge or a single low trough is observed. However, it is more likely that the Moiré is showing a high protruding ridge.

# 7.4.2 One-Dimensional Speckle Interferometry Results

Tests were performed on two tubes with hoop wrinkles, III-7 and III-8. Different fields of view were used, zones 2.2 in. x 2.0 in. and 2.6 in. x 2.0 in., respectively, for the two tubes.

Tube III-8 was the first sample tested. On the first pressurization, 6 fringes of deformation were observed for a 110-psi change. Subsequently, after cycling pressures up to 110 psi, a 10-psi change would cause 13 fringe changes. This pattern of tube deformations was also observed as a permanent change as documented for Tube III-7. Images for Tube III-8 pressurized after many cycles of 100 psi are very similar to the 100-psi case for tube III-7 as in Figure 7.5(B). It should be noted that when non-uniform thickness is used, that this type of behavior change can be expected.

On tube III-7, a more regular pressurization schedule was employed using incremental steps of 100 psi to observe phenomena of material yielding. Pressure differences of 5 to 10 psi were used between the images that would be subtracted to form the fringes. Under these conditions, clear evidence for non-uniform deformations were observed up to 400 psi. An asymmetric deformation is seen from 200 psi on up, reflecting the asymmetry of the hoop lay-up. (Figure 7.5). This was confirmed by looking at the backside (Figure 7.6). Here the fringes were running in a near vertical direction perpendicular to the tube axis and show no asymmetry. That is, the deformation in the hoop direction causes the wrinkled, defect side of the tube to stretch out and to bend the tube ends towards the backside of the tube. The fringe observations are consistent with this interpretation.

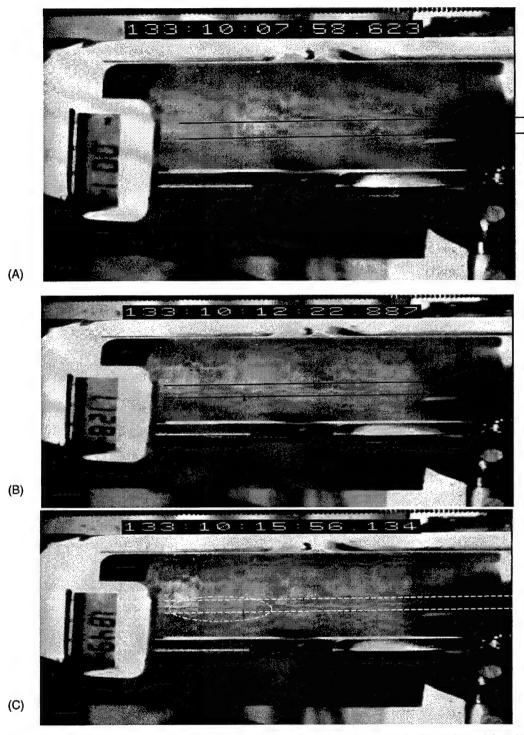


Figure 7.4. Moiré image of size 2.8 in. (v) and 8 in. (h). The dashed lines indicate the rod forming the hoop defect. There are periodic discontinuities formed by steps in the outer epoxy coat from a helical tape wrap. Pressures are (A) 0 psi, (B) 1500 psi, and (C) 2500 psi. The elliptical zone in (C) is where this tube eventually burst at 2695 psi. From 1500 psi upward, a ridgeline is observed coinciding with a rod causing the hoop defect. It is on this ridgeline that the sample eventually ruptured.

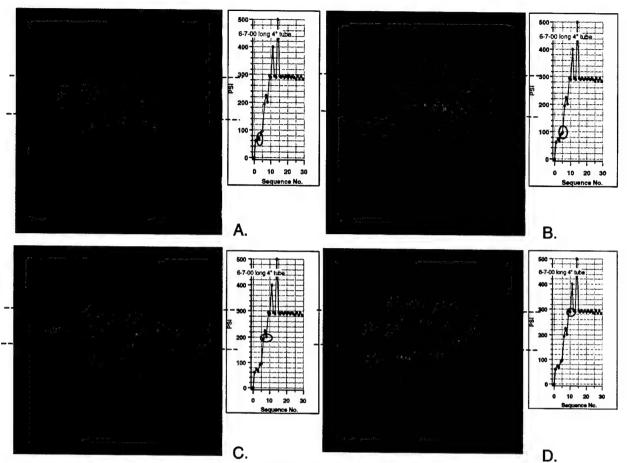


Figure 7.5. Speckle images centered on defect. The image is 6.5 in. (h) x 5.0 in. (v) in size. The dashed horizontal lines marks the location of the rods used for the hoop wrinkles. The plot of pressure on the right of each image is the pressurization history used to obtain the images. Pairs of data points are circled. Pressure difference of (A) 61 and 67 psi, (B) 92 and 98 psi, (C) 194 and 202 psi, (D) 297 and 292. The density of lines is proportional to the pressure difference. Images upon after reaching 500 psi are essentially identical.

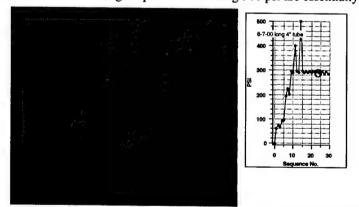


Figure 7.6. Backside of tube opposite the hoop defect. Pressure differences of 297 and 292 psi were used. Again, the pressure history is shown in the graph on the right. Notice the absence of local deformation. Despite a similar pressure difference with Figure 7.5, the number of fringes is significantly smaller, indicating less transverse deformation than the defect side.

During the pressure cycling, loud acoustic pops were heard when 300- and 500-psi pressures were first applied to tube III-7. The tube deformation pattern changed markedly after the 300-psi pop. Similar behaviors with regard to sudden deformation changes were observed for the shadow Moiré deflections in this pressure region. These sudden changes indicate a yielding of the surface, which is probably caused by local bending in the non-uniform thick regions of the sample.

### 7.5 Improvements to Speckle Interferometry of Composite Tubes

In this section, we describe improvements to the speckle interferometer system to allow measurement of 3-dimensional deformations. Since the general deformation of the tube surface occurs in three dimensions during pressurization, and the speckle interferometer images measure deformations along the line of sight of the camera viewing the surface, additional spatial deformation components are needed to derive the three spatial components of the general deformation. It was decided to use three identical imaging cameras, each at a different spatial orientation. The alternate would be to use a single camera nearly on-axis with the tube to measure the transverse deformations and another on-axis system designed for measurement along the direction of observation.

The speckle system was also improved by adding capability to take additional measurements using phase steps in one leg of the interferometer. The four speckle images obtained by subtraction of the raw data, each at a unique phase setting, can then be analyzed to yield phase or deformation maps of the surface.

This section reports experiments using Tube # IV-6, a 12-ply tube with a major helical wrinkle introduced by using three hoop rings. Although the intent of the fiber lay up was to introduce a helical wrinkle, the microscopy of the tube cross section showed that hoop thinning also occurred.

Speckle interferometry requires a well-controlled pressurization environment that is free of other sources of motion during the data collection. The decision was made to mount the experiment on an optical table along with a pressurization system and a box capable of containing debris from a tube under pressurization using liquid (glycol) and a bladder in the tube. The pressurization system is capable of providing up to 5200 psi using a pressure accumulator.

## 7.5.1 The 3-D Speckle System

A simple geometry for a beam reflected off a plane surface as shown in Figure 7.7 can be used to estimate the out-of-plane deformation that is observed in the direction of observation. It is assumed that the speckle reflects light into a wide solid angle. We also assume that only a single speckle spot is present. We need not worry about the details of how the phase varies across the a cylindrical surface since a subtraction of images before and after deformation are used, resulting only in the phase change that occurs due to deformation. Hence, the phase difference  $(\delta)$  in the path the beam takes to the camera can be simplified to the following:

$$\delta = (1 + (\cos \theta)^{-1}) 2 \pi L(u,v,w)/\lambda,$$

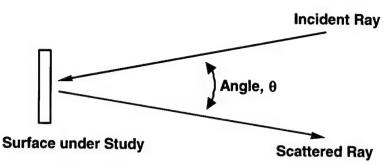


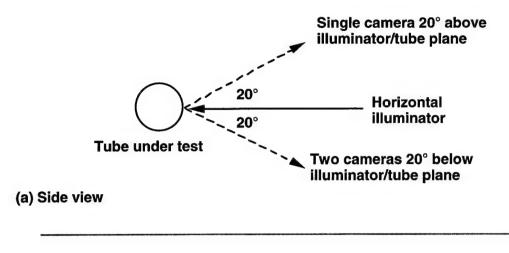
Figure 7.7. Geometry of speckle scattering.

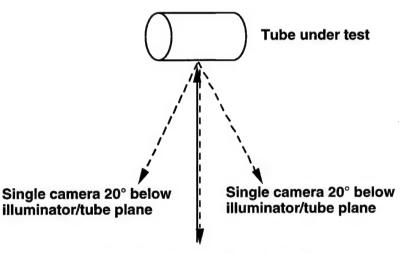
where L is the deformation along local coordinate orthogonal coordinates u, v, and w representing the direction of observation or the scattered ray direction, and  $\theta$  is the angle between the incident and scattered rays. In this approximation, we can neglect the deformation along the u and v directions (w is along the observation direction) for the following reason. In this approximation, it is assumed that the reference wave, which interacts with the scattered ray at the face of the camera on the sensing elements, is near normal, with its phase fronts parallel to the camera face. Also, at the surface under study, the phase fronts are parallel to the front surface. For a plane surface and where the angle  $\theta$  is zero over the entire surface, the phase difference,  $\delta$ , will be a map of the out-of-plane deformation. But since we are using a three-dimensional mapping, there is a possibility that transverse motion will also cause phase changes. An additional consideration is that the viewing angle from the camera to the surface is not always normal for a cylindrical tube of small radius. Hence, the results will be dependent on the orientation of the surface to the camera viewing angle. A sensitivity analysis is needed to place restrictions on the permissible geometrical angles and the maximum error introduced from these effects.

In the geometry selected, two cameras are located in a plane canted 20° below the horizontal plane defined by the tube axis and the illuminator beam. These two cameras are symmetrically oriented relative to the tube at an angle of 90° to one another in the plane. The third camera is located above the illuminator plane at an angle of 20°. A grid of lines spaced by 1 cm provides a spatial reference to correlate positions from each camera on the surface of the tube under test. The locations are sketched in Figure 7.8.

The surface of the tube was spray painted using aluminum paint, which contains metal flakes. Use of ordinary white paint is not recommended due to multiple scattering and the resultant loss of polarization. Aluminum paint preserves polarization. Polarizers were placed before lenses used to image the tube onto the cameras. Two of the cameras were the model 2122 and the third was model 4915 from Cohu. They were ordered with the faceplate removed such that interference fringes from the surface of the faceplate are absent. The cameras all have identical 1/2-in. focal-plane arrays of  $768(H) \times 494(V)$  pixels with high signal-to-noise (>55dB). The pixels dimensions are  $8.4 \mu m$  (H) and  $9.8 \mu m$  (V). Image data was recorded by a National frame grabber, model PCI-1411, using NI IMAQ image acquisition software.

Early experiments indicated that the reflectivity of the painted surface was a strong function of the scattered viewing angle. For the camera geometry described above, there was a noticeable decrease in reflectivity and consequently speckle intensity at the camera. Although the use of faster lenses





Single camera 20° above illuminator/tube plane. Solid arrow defines illuminator plane with tube axis.

# (b) Top view

Figure 7.8. Two projections of the geometry of 3-D speckle tube and camera imaging locations. (a) Side view and (b) Top view.

may improve the signal, the use of faster lenses decreases the speckle size relative to the pixel size. This results in lower sensitivity due to the speckle statistics. We found that satisfactory results can be obtained when the pixel size is several times larger than the speckle spot (assumed to be diffraction-limited). To increase the signal level, gain adjustments and the use of a higher power HeNe laser were deemed necessary. An air cooled  $Ar^+$  laser was used in an attempt to increase the signal, but vibrations introduced by the cooling fan reduced our ability to observe fringes. A 10-mW HeNe laser would increase signals by an order of magnitude and still keep an acceptably long coherent path of 10 cm. The coherence length is the allowable path difference over which pieces of a beam will continue to show interference with one another.

# 7.5.2 Phase Measurement and Phase Stepping

Several methods were investigated for the determination of deformation or phase change due to the displacement caused by a small pressure increment and sensed by all three cameras. The method used is the three phase steps in which the phase of the reference leg is changed by equal phase steps of  $2\pi/4$  using a piezo-mirror translator, model P-802.11 from Polytec. The method consists of obtaining 4 images with, and 4 images without the pressurization-induced deformation. These images are used to form four interference patterns. These images are then Fourier filtered to normalize and to remove the high spatial frequency of the speckle. The Fourier filter is selected such that the filtered image shows overlap of adjacent speckles and hence "smoothing." The 4 processed subtracted images are then combined to give the phase angle for the deformation phase,  $\alpha(x,y)$ .

$$\alpha(x,y) = \arctan \{ [I_3(x,y) - I_1(x,y)] / [I_0(x,y) - I_2(x,y)] \},$$

where the image  $I_n(x,y)$  labels the four filtered images with an index of n for a phase step of  $\pi/2$ . This method of phase steps and filtering has the advantage of eliminating uneven illumination, contrast variations, etc. Steps must be taken to remove the  $2\pi$  ambiguity that results. A procedure, not yet incorporated, that solves this problem uses a min-max routine and determines the sign of the phase by adding a known phase shift and analyzing the intensity shift that results.

The Fourier filtering of the four images is performed by taking the forward Fourier transform of the image and multiplying the result with a mask such that the "origin" of the transform is zeroed out, but the region around it is kept. The size of the non-zero region corresponds to the modulation transfer function of a lens that reduces the resolution of the original image. The mask zeros out all other higher frequency components and is, hence, a low-pass convolution. Details are described in Ref. 7.3.

The result of using the three step or four image method is shown in Figure 7.9 for a hollow composite tube in which a deformation is produced by placing a wrench of a few pounds into the center of the tube. This phase image was measured by the camera on the lower left side as one faces the tube from the position of the illuminator beam. It represents the projection of deformation in the direction of the viewing camera. The tube is supported by a cradle beneath the tube by two "vee" blocks. In the upper part of the image corresponding to the lower part of the tube, a modest amount of deformation is seen. Each fringe corresponds to  $\lambda/2$  change along the camera's line of sight that is out of the plane of the image.

# 7.5.3 Status of Speckle Interferometry Upgrades

A series of images of tube IV-6 with a major helical wrinkle undergoing deformation were taken at 1000, 2000, 3000, and 4000 psi. In each series, small increments of pressure of 20–30 psi were taken over a 100-psi span centered on the thousand psi large step. No fringes could be observed. Yet, when a hollow tube was used, fringes could be observed with the identical set-up. Hence, it was concluded that the tube was deforming with large deformations and that the fringes were washed out. The support for the tube consists of a dual "V" block fixture placed under the tube under test. It is thought that the V block is not capable of providing the stability to observe fringes. A cradle support design is proposed as a solution.

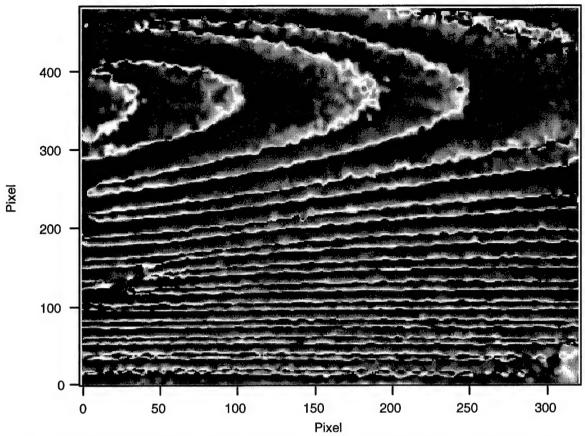


Figure 7.9. The phase of an empty graphite epoxy tube deformed by placing a wrench into the center of the tube. The image is switched around, upside-down and left to right. The motion of the tube is complex. Fringes in the lower right corner are not well defined due to poor signal levels. The phase is shown as varying from 0 to  $2\pi$  as the intensity is modulated from 0 to 256 gray scale. The field of view is about 5.0 x 6.0 cm on the tube.

### 7.5.4 Conclusion of Speckle Interferometry Upgrades

The speckle interferometry was configured for 3-dimensional deformation measurements using 3 cameras placed at 3 locations to measure the projected deformation in each direction. Although fringes were not observed, improvements to the system were implemented or proposed to measure the deformations. A high-pressurization system was installed. A sensitivity analysis was identified that would delineate the relative effects of transverse to out-of-plane phase change. Many of these fixes can be readily achieved.

### 7.6 Conclusions

Both optical methods, shadow Moiré and speckle interferometry, show good potential for studying pressurization effects and mechanisms that may determine the ultimate burst strength of the tubes. With further effort, the diagnostics could be used to validate predictions of burst strength, to validate models, and perhaps to provide a unique diagnostic that could be used on large-scale tube structures. With both techniques, unexpected mechanisms were observed. One is the sudden popping phe-

nomena of a local deformation during first-time pressurization in the vicinity of the non-uniform thickness sample zones that undergo a bending yield. The observations of localized strain are consistent with asymmetric lay-up of hoop wrinkles. The backside also yields information about the deformations of the tube induced by the wrinkles. There seems to be a global bending of the tube when the defects are restricted to one side of the tube.

Some improvements for the Moiré are to smooth the surface to reduce the effects of discontinuities in the surface due to tape wraps. This was demonstrated by sanding and repainting the surface such as to not affect the external fiber wrap layers. Correlation of acoustic emission and acoustic transducer data to the fringe behavior are also likely to yield further insight into tube behavior during pressurization. Tests at higher pressures are needed for the speckle interferometry and more sensitive pressure instrumentation due to the high sensitivity of speckle interferometry.

One issue that needs resolution for application to new, undiagnosed, or untested samples is what the test pressure must be relative to the burst pressure such that the observed deformations indicate the presence of a defect and not a local relaxation. For the tube observed during the Moiré burst testing, the tube ideal strength was 3000 psi; the defect design was 2000 psi or 67%, and measured was 2675 or 89%. It appears that at 1500 psi, the defect location appeared to be stable. For this geometry, pressurization to 50% appears to be sufficient. However, if local bending is needed for tubes or samples with larger thickness variations, larger pressure changes may be needed, and hence higher pressures are necessary.

Since we have observed anomalous deformations, we can conclude that even with the small number of samples, the use of optical diagnostics may also lead to checks on workmanship and design and to more robust designs of graphite-epoxy pressure vessels in the future.

### 8. Observations and Conclusions

Although we did not do a statistically significant number of experiments, there are two strong trends in the data that are worthy of mention:

- 1. Proof pressures up to ~95% of burst and number of proof testing cycles had no noticeable effect on the average ultimate burst pressures of the tubes. With only one exception, all of the tubes burst at a higher pressure than the proof pressures applied. The lone sample that failed at a lower pressure was proofed three times to 98% of the average burst pressure and failed at a pressure about 0.2% lower than the pressure applied for the three prior proof cycles.
- 2. The burst strengths of the tubes with no wrinkles that were studied in this program were designed to be dominated by the hoop fibers. For these tubes, minor helical wrinkles had no measurable effect on the burst pressure. More severe helical wrinkles caused an average reduction in burst pressure of 8%. Hoop wrinkles caused a significant degradation in strength (14% on average).

#### Some other observations:

- All of the tubes, with one exception, failed as the pressure level was increasing. One tube failed 5 s into a hold cycle. There was no significant acoustic activity detected during this hold.
- The failure initiation points were determined by examining the high-speed camera images. In the tubes with wrinkles, all failures initiated in the immediate vicinity of the wrinkles. All the failures occurred either in the membrane area (no defects) or in the vicinity of the fabricated defects. No effects from the end fittings were observed.
- Acoustic emission data showed no large-energy events that corresponded to
  delaminations or fiber breaks during pressure holds. However, many low-energy events
  corresponding to growth of microcracks at the microscale level were recorded during
  initial pressurization. All of the tubes were quiet when re-pressurized to equivalent
  pressures.
- Acoustic emission monitoring provided an excellent method for discriminating between
  tubes with a nominal burst pressure and those that burst at low pressure. The tubes that
  burst low (i.e., tubes with hoop wrinkles) exhibited more higher-energy events at low
  pressures than their nominal counterparts.

- Linear finite-element analyses of the tubes with wrinkles produced mixed results. On the one hand, analysis of the tubes with severe helical wrinkles produced quite good agreement with experiments. The measured drop in burst strength was roughly 8%, while the predicted drop was 12%. However, the finite-element analysis of the tubes with hoop wrinkles overestimated the strength reduction due to fiber misalignment.
- Shadow Moiré identified the role of known hoop defects leading to rupture. In addition, unusual flexing of the tube surfaces during low-pressure inflation was noted. This indicates that local shape changes take place well below the burst limit, especially in areas associated with defects. These deformations were also observed using speckle interferometry. These two optical diagnostic techniques hold promise for identifying potential critical defects in a tube well below its burst limit, and could lead to new techniques for the identification of critical defects during the proof testing of composite pressure vessels.

It is not clear whether the growth of microcracks at low pressures seen in the acoustic emission, shadow Moiré, and speckle interferometry data is significant. Also unknown is whether it is beneficial or detrimental to the ultimate tube strength. These microcracks might weaken the tubes sufficiently to cause lower burst pressures. Alternatively, they might blunt the stress concentrations within the composite and somewhat mitigate the effect of the fiber wrinkles. More work is required to better understand this phenomenon.

### References

- 3.1 D. J. Chang, P. R. Valenzuela, and T. V. Albright, "Burst Tests of Filament-wound Graphite-epoxy Tubes Pathfinder Test Series For Delta II GEM Motor Cases," Aerospace Report No. TR-2000(1494)-1, The Aerospace Corporation, 20 Dec 2000.
- 3.2 D. J. Chang, and P. R. Valenzuela, "Pressure Vessel Testing Fixture," US Patent # 6253599, July 3, 2001.
- 6.1 L. A. Carlsson and R. B. Pipes, *Experimental Characterization of Advanced Composite Materials*, Prentice Hall, 1987, pp. 13–15.
- 7.1 M. C. Shellabear and J. R. Tyrer, "Application of ESPI to Three-Dimensional Vibration Measurements," *Optic and Laser in Engineering*, **15**, 43-56(1991).
- 7.2 A. J. Moore and J. R. Tyrer, "Surface Strain Measurement with ESPI Applied to Fracture Mechanics," Hologram Interferometry and Speckle Metrology, proceedings of SEM, 192-198(1990).
- 7.3 E. Vikhagen, "Nondestructive Testing by Use of TV Holography and Deformation Phase Gradient Calculation," *Appl. Optics*, **29**, 137-144(1990).